



**HAL**  
open science

## Subducting slabs: jellyfishes in the Earth mantle

Christelle Loiselet, Jean Braun, Laurent Husson, Christian Le Carlier de Veslud, Cédric Thieulot, Philippe Yamato, Djordje Grudjic

► **To cite this version:**

Christelle Loiselet, Jean Braun, Laurent Husson, Christian Le Carlier de Veslud, Cédric Thieulot, et al.. Subducting slabs: jellyfishes in the Earth mantle. *Geochemistry, Geophysics, Geosystems*, 2010, 11 (8), pp.Q08016. 10.1029/2010GC003172 . insu-00609425

**HAL Id: insu-00609425**

**<https://insu.hal.science/insu-00609425>**

Submitted on 9 Jun 2017

**HAL** is a multi-disciplinary open access archive for the deposit and dissemination of scientific research documents, whether they are published or not. The documents may come from teaching and research institutions in France or abroad, or from public or private research centers.

L'archive ouverte pluridisciplinaire **HAL**, est destinée au dépôt et à la diffusion de documents scientifiques de niveau recherche, publiés ou non, émanant des établissements d'enseignement et de recherche français ou étrangers, des laboratoires publics ou privés.



## Subducting slabs: Jellyfishes in the Earth's mantle

### Christelle Loiselet

*Géosciences Rennes, UMR 6118, Université de Rennes 1, CNRS, F-35042 Rennes, France*

*Now at Mineral Resources Division, BRGM, 3 avenue Claude Guillemin, BP 6009, F-45060 Orleans CEDEX 2, France (c.loiselet@brgm.fr)*

### Jean Braun

*Géosciences Rennes, UMR 6118, Université de Rennes 1, CNRS, F-35042 Rennes, France*

*Now at Laboratoire de Géodynamique des Chaînes Alpines, Université Joseph Fourier de Grenoble, F-38041 Grenoble, France (jean.braun@bvara.ujf-grenoble.fr)*

### Laurent Husson

*Géosciences Rennes, UMR 6118, Université de Rennes 1, CNRS, F-35042 Rennes, France*

*Also at Laboratoire de Planétologie et Géodynamique de Nantes, UMR 6112, CNRS, F-44322 Nantes, France (laurent.husson@univ-rennes1.fr)*

### Christian Le Carlier de Veslud

*Géosciences Rennes, UMR 6118, Université de Rennes 1, CNRS, F-35042 Rennes, France (christian.le-carlier@univ-rennes1.fr)*

### Cedric Thieulot

*Department of Earth Science, University of Bergen, N-5020 Bergen, Norway (cedric.thieulot@geo.uib.no)*

### Philippe Yamato

*Géosciences Rennes, UMR 6118, Université de Rennes 1, CNRS, F-35042 Rennes, France (philippe.yamato@univ-rennes1.fr)*

### Djordje Grujic

*Department of Earth Sciences, Dalhousie University, Halifax, Nova Scotia B3H 4J1, Canada (dgrujic@dal.ca)*

[1] The constantly improving resolution of geophysical data, seismic tomography and seismicity in particular, shows that the lithosphere does not subduct as a slab of uniform thickness but is rather thinned in the upper mantle and thickened around the transition zone between the upper and lower mantle. This observation has traditionally been interpreted as evidence for the buckling and piling of slabs at the boundary between the upper and lower mantle, where a strong contrast in viscosity may exist and cause resistance to the penetration of slabs into the lower mantle. The distribution and character of seismicity reveal, however, that slabs undergo vertical extension in the upper mantle and compression near the transition zone. In this paper, we demonstrate that during the subduction process, the shape of low viscosity slabs (1 to 100 times more viscous than the surrounding mantle) evolves toward an inverted plume shape that we coin *jellyfish*. Results of a 3D numerical model show that the leading tip of slabs deform toward a rounded head skirted by lateral *tentacles* that emerge from the sides of the *jellyfish* head. The head is linked to the body of the subducting slab by a thin tail. A complete parametric study reveals that subducting slabs may achieve a variety of shapes, in good agreement

with the diversity of natural slab shapes evidenced by seismic tomography. Our work also suggests that the slab to mantle viscosity ratio in the Earth is most likely to be lower than 100. However, the sensitivity of slab shapes to upper and lower mantle viscosities and densities, which remain poorly constrained by independent evidence, precludes any systematic deciphering of the observations.

**Components:** 13,000 words, 11 figures, 2 tables.

**Keywords:** subduction; slab viscosity; mantle stratification; seismic tomography.

**Index Terms:** 8170 Tectonophysics: Subduction zone processes (1031, 3060, 3613, 8413); 8148 Tectonophysics: Planetary volcanism (5480, 8450); 0545 Computational Geophysics: Modeling (1952, 4255).

**Received** 13 April 2010; **Revised** 8 June 2010; **Accepted** 23 June 2010; **Published** 20 August 2010.

Loiselet, C., J. Braun, L. Husson, C. Le Carlier de Veslud, C. Thieulot, P. Yamato, and D. Grujic (2010), Subducting slabs: Jellyfishes in the Earth's mantle, *Geochem. Geophys. Geosyst.*, *11*, Q08016, doi:10.1029/2010GC003172.

## 1. Introduction

[2] The wide range of shapes observed among subducting oceanic lithospheres [Isacks and Molnar, 1971; Kárason, 2002; Li et al., 2008] suggests a complex dynamical behavior for the penetration of slabs into the mantle. The lack of earthquake activity below 700 km depth and the compressive nature of the focal mechanisms of the deep earthquakes along the surface of the slabs have been interpreted as an effect of the resistance of slabs to penetration into the lower mantle [Isacks and Molnar, 1971]. Such observations are at least compatible with dynamic models of the long wavelength geoid anomalies associated with slabs requiring an increase in viscosity from the upper to the lower mantle by a factor 10–100 [Hager and Richards, 1989; Lambeck and Johnston, 1998; Moresi and Gurnis, 1996; Peltier, 1996; Ricard et al., 1993] or more [Kido and Cadek, 1997]. But travel time tomography has also revealed that positive seismic anomalies attributed to slabs often extend into the lower mantle [Creager and Jordan, 1986; Grand, 1994; Jordan, 1977; Jordan and Lynn, 1974]. In the last decade, images from seismic tomography have improved in resolution and accuracy, and have revealed that slabs tend to thicken during penetration into the lower mantle, i.e., from the transition zone to mid-mantle depths [Bijwaard et al., 1998; Fukao et al., 2001; Grand et al., 1997]. Examples thereof include the Central and South Americas [Ren et al., 2007], southern Asia [Kárason, 2002; Li et al., 2008] or the Hellenic slab [Piromallo and Morelli, 2003; Wortel and Spakman, 2000]. Slab thickening in the mid-lower mantle is often interpreted as evidence for periodic buckling of cold and stiff lithosphere as it penetrates

into the mantle [Gaherty and Hager, 1994; Guillou-Frotier et al., 1995; Loubet et al., 2009; Ribe et al., 2007]. However, the deformation of slabs going sinking through the mantle has also been interpreted as evidence that subducting plates could be very weak [Bevis, 1986; Čížková et al., 2002; Giardini and Woodhouse, 1984; Tao and O'Connell, 1993]. Indeed, although they have not emphasized this aspect before, previous authors [e.g., Christensen and Yuen, 1984; Zhong and Gurnis, 1995; Funicello et al., 2003] do simulate (via numerical and analog modeling) comparable spherical shapes for weak descending plates. Only Kárason [2002] effectively associated the seismically observed morphology of slabs penetrating into the deep mantle to that of a thickened isoviscous slabs. He showed that the thickening of weak subducting slabs changes systematically with the viscosity contrast between the upper and lower mantles.

[3] Furthermore, the viscosity of the subducting plate strongly influences plate deformation and therefore its dynamics. In the literature, the range of assumed and predicted viscosity ratios between the slab and the surrounding mantle is large, comprised between  $10^6$  [Kincaid and Griffiths, 2003] and 1 [Husson, 2006; Kárason, 2002]. The values used in recent models are comprised between  $10^2$  and  $10^3$  [Clark et al., 2008; Faccenna et al., 2001; Funicello et al., 2003; Schellart, 2004; Stegman et al., 2006; Yamato et al., 2009]. Previous work from Loiselet et al. [2009] suggested that the viscosity ratio should be smaller than  $10^2$ .

[4] In view of these most recent estimates of the viscosity ratio between the subducting plate and the surrounding mantle, we expanded on Kárason's

[2002] work, exploring the possibility that a plate sinking into the mantle deforms and naturally thickens at mid-depths, without the need for a stiff lithosphere or a viscosity or density jump in the lower mantle. To demonstrate this point, we investigate here the role of the viscosity ratio between the plate and the surrounding fluid and, subsequently, the role of mantle stratification (corresponding to a viscosity or density jump) in forming a wide range of shapes, ranging from that of an undeformed slab to the characteristic shape of a downwelling plume that we refer to as a *jellyfish*. In the latter part of this paper, we further discuss our results in light of observed slab geometries, which we extract from seismic tomography images.

## 2. Methodology

[5] In order to explore the dynamic interactions between the subducting lithosphere and the surrounding viscous mantle, we evaluate the deformation pattern of a slab sinking into the mantle by means of a three-dimensional numerical model that is designed to track sharp, dynamically deforming interfaces. The 3D finite element code *DOUAR* [Braun et al., 2008] solves for the conservation equations for mass, momentum and energy in the Boussinesq approximation, assuming that the mantle is an incompressible viscous medium. *DOUAR* is an ALE (Arbitrary Lagrangian Eulerian) Finite Element code based on an adaptive octree grid [Thieulot et al., 2008] that is highly suited to solve geometry problems in three dimensions. An octree is the simplest hierarchical division of the unit cube into smaller cubes, obtained by dividing, where higher resolution is required, each cube into 8 smaller cubes, up to a given or desired resolution. The smallest or undivided cubes are called the “leaves” of the octree. In *DOUAR*, the computational domain is therefore a unit cube, the finite elements are the leaves of the octree and their density is adapted to represent the various material, density and viscosity interfaces with optimum accuracy. The flow is driven by the internal density difference  $\Delta\rho$  between the subducting lithosphere and the surrounding mantle. We simplify our analysis by assuming an infinite Prandtl number in a fluid with very low Reynolds number ( $Re = 0$ ) and a linear rheology for all components of the system. Under such conditions, the velocity field  $\mathbf{u}$  and pressure  $p$  obey the following simplified form of Navier–Stokes equations, referred to as the Stokes equations:

$$\nabla \cdot \mu (\nabla \mathbf{u} + \nabla \mathbf{u}^T) - \nabla p = \rho \mathbf{g} \quad (1)$$

and

$$\nabla \cdot \mathbf{u} = 0 \quad (2)$$

where  $\rho$  is the density,  $g$  the gravitational acceleration,  $p$  the pressure field,  $\mu$  the dynamic viscosity and  $\mathbf{u}$  the velocity.

[6] Interfaces (between the slab, upper mantle and lower mantle) are advected by using the computed velocity field and are tracked by a dual method combining Lagrangian particles for accuracy and level set functions for efficiency (see Braun et al. [2008] for further details on this method).

[7] The model setup is shown in Figure 1a and parameters are given in Table 1. The computational numerical domain is a unit cube (i.e.,  $1 \times 1 \times 1$  in  $x, y, z$  directions) representing a  $\sim 2750$  km Cartesian box, corresponding to the Earth’s mantle. The mantle is divided between an upper and lower mantle where a material discontinuity (i.e., that is advected with the flow) is imposed at  $z_{660} = 0.24$  ( $\sim 660$  km). The grid counts  $(64)^3$  (or level 6 octree) regularly spaced elements (or leaves) everywhere but in and around the slab where the resolution is increased to level 8, i.e., the element size is  $1/256$  of the size of the unit cube. Free slip is assumed on all boundaries. The experiment is initiated by placing a vertical (unless otherwise specified) plate of length,  $l = 0.066$  ( $\sim 182$  km) and thickness  $h = 0.03$  ( $\sim 83$  km) in the mantle between depths of 0.03 and 0.096 ( $\sim 83$  km to 264 km, Figure 1a).

[8] To ensure that the plate falling is controlled only by the buoyancy forces arising from the density contrast and by the viscosity ratio between the plate and the surrounding viscous fluid, the velocity at the top boundary of the plate is not fixed (i.e., not set to zero for the calculation of the velocity field). For the same reason, the top boundary of the slab is not attached to the top of the model box where the velocity component in the  $z$ -direction vanishes (free-slip conditions). However, since the slab is considered “infinite” in our simulation, slab material is constantly added from the top. To simulate that, we do not update the geometry of the upper boundary of the slab from the computed velocity field, such that it stays at the same level through time (i.e., at  $z = 0.03$  from the top of the model box). Consequently, plate volume increases with time. In this way we discard any resistance to sinking that may arise in nature from the relative horizontal movement between the plate and the mantle. We assign a constant density contrast between the slab and the surrounding mantle. All viscosities are Newtonian and uniform within the slab and the

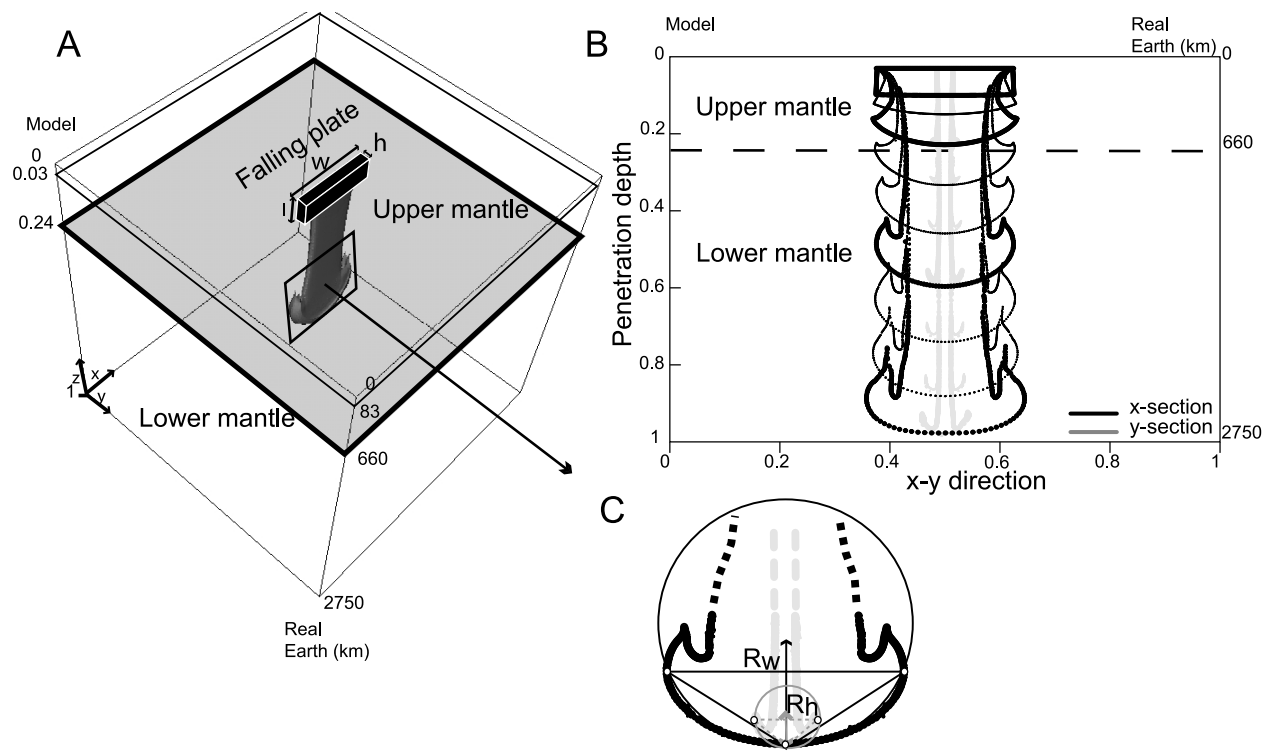


**Figure 1.** Reference model. (a) Model setup and variables:  $h$  is plate thickness,  $w$  is plate width,  $l$  is initial plate penetration. The black parallelepiped is the initial slab geometry and the gray body is a typical slab shape after subduction to mid-depth. (b)  $x$ - (black) and  $y$ - (gray) cross-section series of the plate at different stages (uniform time steps). Bold profiles denote notable stages (see text). (c) Vertical cross section along the  $x$ - (black) and  $y$ - (gray) sections of the leading edge of the subducting plate.  $R_w$  (black) (measured along the width  $w$  of the plate) and  $R_h$  (gray) (measured along its thickness  $h$ ) give the radii of the circles that circumscribe the dotted triangles.

mantle; the upper mantle viscosity is taken as the reference viscosity ( $= 1$ ). More complex rheologies may prevail in nature, especially rheologies that account for the influence of temperature on viscosity

[e.g., *Billen and Gurnis, 2005*], but we chose to keep the model as simple as possible in order to quantify its behavior as a function of the effective slab to mantle viscosity ratio that we vary from  $\mu_s = 0.01$  to

**Table 1.** Parameters Used in the Models

Description	Parameter	Model	Nature
<i>Slab</i>			
Thickness	$h$	0.03	~83 km
Width	$w$	0.125/0.25 <sup>a</sup> /0.5	344/688/1375 km
Dip angle	$\alpha$	90 <sup>a</sup> /70/45/30	90 <sup>a</sup> /70/45/30
Density	$\rho_s$	0.1024	~3328 kg.m <sup>-3</sup>
Viscosity ratio	$\mu_s$	10 <sup>-2</sup> /10 <sup>0</sup> /10 <sup>1a</sup> /10 <sup>2</sup>	10 <sup>-2</sup> /10 <sup>0</sup> /10 <sup>1a</sup> /10 <sup>2</sup>
Uniform octree level	$L_s$	8 (0.0039)	~10.72 km
<i>Upper Mantle</i>			
660 km boundary	$z_{660}$	0.24	660 km
Density	$\rho_{um}$	0.1	~3250 kg.m <sup>-3</sup>
Viscosity	$\mu_{um}$	1	2.10 <sup>-20</sup>
Uniform octree level	$L_{um}$	6 (0.0156)	~43 km
<i>Lower Mantle</i>			
Density	$\rho_{lm}$	0.1 <sup>a</sup> /0.1012/0.1024/0.1032	~3250 <sup>a</sup> /3289/3328/3434 kg.m <sup>-3</sup>
Viscosity ratio	$\mu_l$	10 <sup>0a</sup> /10 <sup>1</sup> /10 <sup>2</sup> /10 <sup>3</sup>	10 <sup>0a</sup> /10 <sup>1</sup> /10 <sup>2</sup> /10 <sup>3</sup>
Uniform octree level	$L_l$	6 (0.0156)	~43 km

<sup>a</sup>Reference value.

100. In our study, plate width,  $w$ , and initial slab dip,  $\alpha$ , are also varied between 1/8, 1/4, and 1/2 of the box width and 90, 70, 60, 45 and 30° respectively.

### 3. Results

[9] We performed a series of 27 experiments to explore the dependence of the slab deformation on slab to lower mantle density contrast  $\Delta\rho$ , slab width  $w$ , slab dip  $\alpha$ , slab to mantle viscosity ratio  $\mu_s$ , and lower to upper mantle viscosity ratio  $\mu_l$ . Some interesting features prevail regardless of the parameter values that we review below. To illustrate this point, we first show the results of a simple experiment (reference model) in which the plate viscosity is 10 times that of the upper mantle and where there is no viscosity or density contrast between the upper and lower mantle. The initial plate width is 0.25 (i.e., 1/4 of the box width) and the slab is vertical.

#### 3.1. General Evolution of the Models

[10] During the sinking of the plate into the mantle, its shape evolves in a comparable way, to a large extent, to that of a reverse or descending plume (Figures 1a and 1b) [Christensen and Yuen, 1984; Káráson, 2002]. Note however that in most of our models the viscosity ratio is inverted in comparison to that of a typical rising mantle plume, which is characterized by a lower viscosity than the surrounding mantle. The shape of the slab is characterized by a rounded head at its leading tip, with two trailing “tentacles” along each narrow edge (Figure 1b), and connected to the surface by a long rectangular section tail. The initial rectangular shape probably promotes the development of the tentacles, but even when using plates with smooth edges, they still form. To a minor extent, the mantle also drags the longer edges and gently wraps them over the body of the slab (Figure 1b). In the following, we refer to the deformed shape of the slab as that of a *jellyfish*, for both our model slabs and real jellyfishes are characterized by comparable shapes that should minimize the viscous dissipation of energy while they move through the fluid. The jellyfish shape can be characterized by the longitudinal radius of curvature  $R_w$  and the lateral radius of curvature  $R_h$  (see Figure 1c). In practice, to calculate  $R_w$  and  $R_h$ , we compute the equation of the circle that circumscribes the triangle defined by the three vertices made by the leading tip (deepest point of the greatest  $z$ -value) and the two tips of the tentacles in the longitudinal direction (points of maximum and minimum  $x$ -value

for  $R_w$  and  $y$ -value for  $R_h$ ). To further characterize the shape of the jellyfish and the flow it engenders in the mantle, we compute for each of the numerical experiments: (a) the velocity of the jellyfish head (measured on the slab at its maximum  $z$ -position) and its radius of curvature, (b) the maximum strain rate along the central vertical axis  $z$ , (c) the surface area of horizontal sections of the plate (distant by 0.03) as a function of depth and (d) the total viscous dissipation in the mantle.

[11] During the initial stages of subduction, the slab head becomes wider, thicker and curved (Figures 1b and 2a). The sinking velocity (measured at the jellyfish head) increases with plate deformation (Figure 2a). The radius of curvature  $R_w$  decreases rapidly (Figure 2b) as the slab tip evolves from a straight horizontal edge into a curved body. During this phase both the strain rate (Figure 3a) and the viscous dissipation in the mantle (Figure 3b) increase rapidly. When the slab tip reaches depths of 0.2 to 0.4, the head of the jellyfish is fully developed and an optimal curvature has been reached as indicated by the steady minimal value for  $R_w$  (Figure 2b).

[12] As the slab further penetrates into the mantle, the ratio between the lateral and longitudinal radii increases (Figure 2b), suggesting that the jellyfish head shape evolves toward a sphere (i.e., the radius of curvature is the same in all directions). During this stage, the sinking velocity continues to increase toward a maximum value (Figure 2a), yet the strain rate and mantle viscous dissipation remain steady (Figures 3a and 3b). In fact, once the jellyfish head is formed, only the “tentacles” continue to grow (Figure 1b). A neck forms above the jellyfish head, along the tail connecting the head to the surface (Figure 1b), its area remaining constant. At this stage, the jellyfish head area is respectively 1.5 and 2 times larger than the maximum (which is at the surface) and minimum (at the neck) surface areas of the tail (Figure 3d). According to the distribution of vertical strain (Figure 3c), the tail is lengthened near the surface while the head is shortened at depth (Figure 3c). Consequently, the head perimeter is as enlarged as the tail is thinned with respect to the original dimension of the slab before subduction. The final stage of evolution of the shape of the slab reflects the interaction of the jellyfish with the bottom of the box. The sinking velocity decreases to zero and the jellyfish head flattens.

[13] In the following paragraphs, we show how this general scheme is modulated by variable setup geometries and key parameters, in order to under-

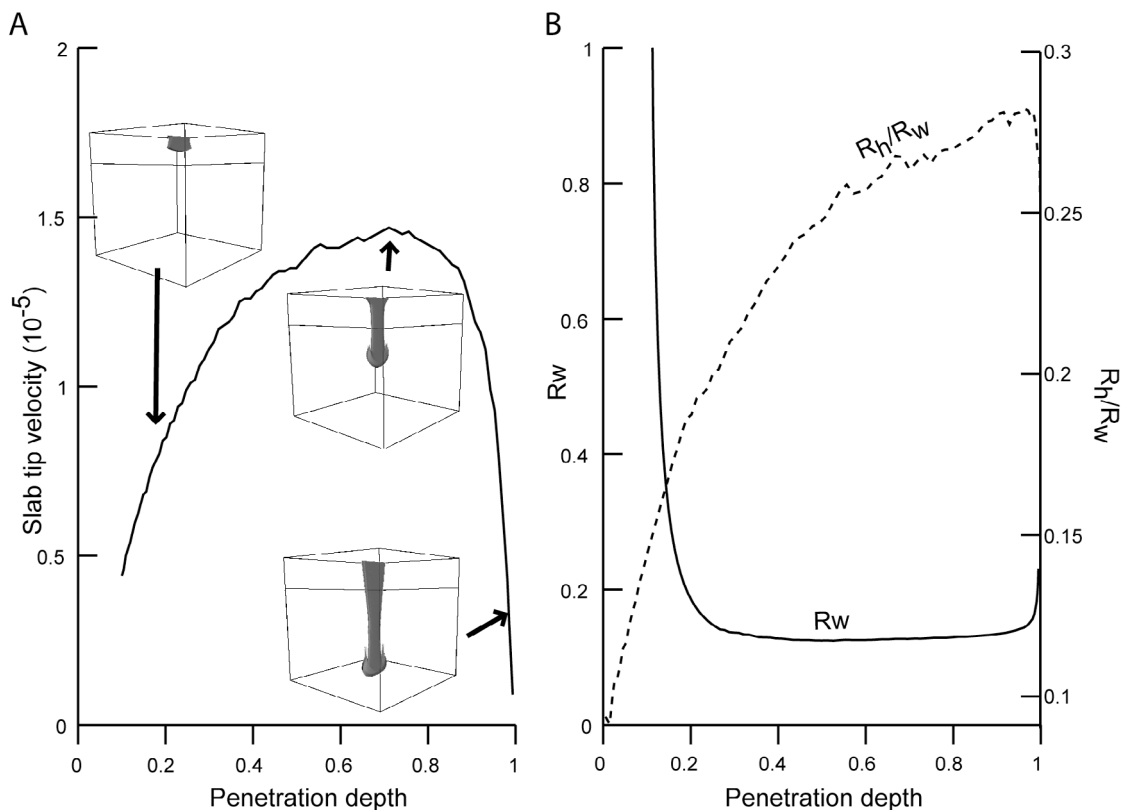


**Figure 2.** Reference model. (a) Velocity of the slab head as a function of penetration depth. (b) Radius of curvature  $R_w$  of the slab head across the  $x$ -profile (solid) and ratio between lateral ( $R_h$ ) to longitudinal ( $R_w$ ) radii of curvature of the jellyfish head (dashed).

stand the processes that control the behavior of the slab as it penetrates into the mantle.

### 3.2. Slab Width

[14] Plate width is known to influence the kinematics of subduction [Di Giuseppe *et al.*, 2008; Loiselet *et al.*, 2009; Piromallo *et al.*, 2006; Schellart *et al.*, 2007]. We evaluate its impact on the shape of the jellyfish by varying the plate width  $w$  between 0.125 and 0.5 (1/8 and 1/2 of the box width) while leaving the box size and plate thickness unchanged. Results show that, in all cases, the radius of curvature  $R_w$  of the jellyfish head decreases through time and tends toward a minimal value (Figure 4a). When normalized to slab width  $w$  and slab thickness  $h$ ,  $R_w$  reaches a value comprised within a narrow range ( $\sim 3/4$ ) proportional to the sum of the width and thickness, i.e., the jellyfish head evolves toward a locally regular, spherical shape with a diameter proportional to  $1.5 * (w+h)$ . This is better illustrated by considering the  $R_h/R_w$  ratio (Figure 4b), which increases with slab penetration. Of course, the ratio between the initial slab width and thickness influences the cur-

vature of the jellyfish head. If the plate has an initial square horizontal cross section, the slab diameter tends to 1 and  $R_w$  is always equal to  $R_h$ . Implicitly, the rate of formation of the jellyfish shape depends on the initial plate shape (i.e.,  $w/h$  ratio): a narrow plate adopts the jellyfish shape faster than a wide plate.

### 3.3. Slab Dip

[15] In most natural cases, subduction does not initiate vertically: slabs tend to dip at a finite angle underneath the overriding plate. We explore the impact of slab dip on the jellyfish evolution by varying its value between 30 and 90°. Boundary conditions are the same as for the reference model. In Figure 5, we present results from two experiments, characterized by slab dips of 60 and 30°, respectively. The radius of the jellyfish head decreases and tends toward a minimal  $R_w$  value, regardless of the initially imposed slab dip. However, the morphology gets highly asymmetrical for shallow dipping slabs and the jellyfish shape transforms into a spoon shape (Figures 5a and 5b). Note that in our numerical

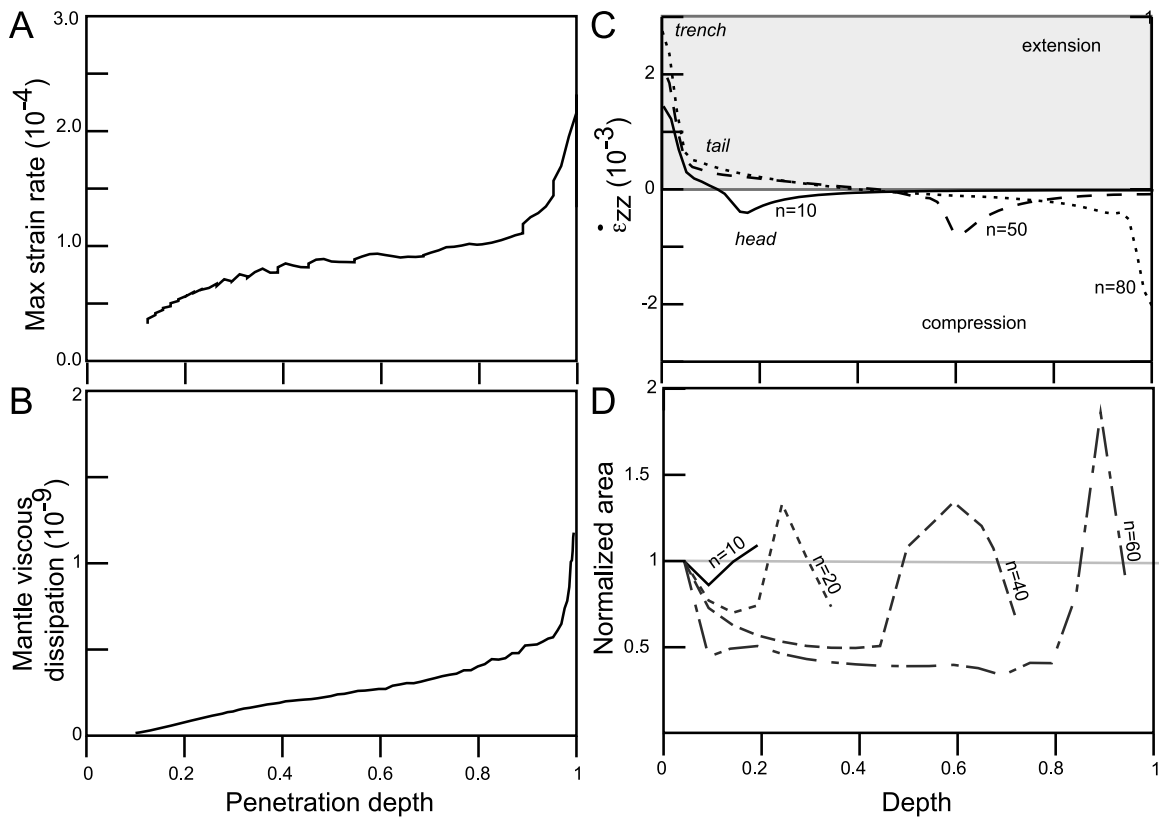


**Figure 3.** Reference model. (a) Maximum strain rate as a function of plate penetration depth. (b) Bulk viscous dissipation in the mantle as a function of plate penetration depth. (c) Vertical strain rate ( $\dot{\epsilon}_{zz}$ ) profile along the central axis of the plate ( $x = 0.5$  and  $y = 0.5$ ) at different time steps  $n$ . (d) Normalized areas of horizontal slab sections as a function of depth, at different time steps  $n$ .

setup, the location of the subduction zone at surface level remains fixed with respect to the underlying mantle while in nature, this may not be the case and slabs may gradually become vertical, thanks to the

advance of the trench and/or retreat of the slab/head (Figures 5c and 5d). The dip does not seem to be a critical parameter in our parametric study and in the following numerical experiments we will only con-

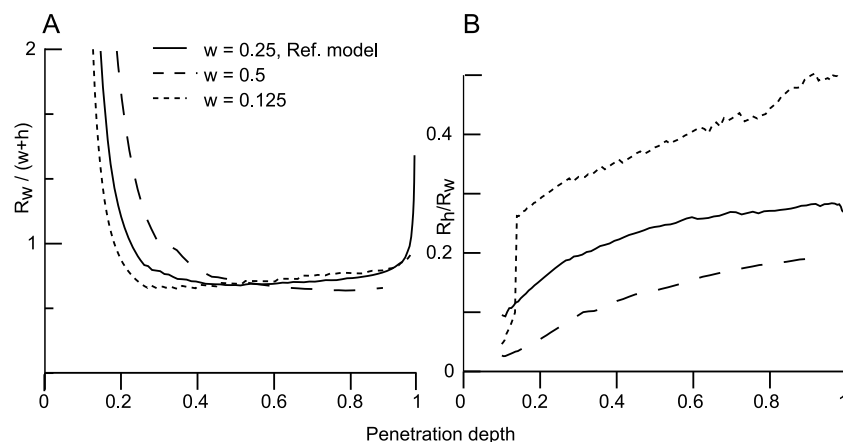


**Figure 4.** Reference model. (a) Radius of curvature  $R_w$  of the jellyfish head as function plate penetration depth, normalized to the sum of slab width  $w$  and slab thickness  $h$  for different slab width  $w$ , 0.25 (solid), 0.5 (dash) and 0.125 (dot). (b) Same as Figure 4a but for the ratio between lateral ( $R_l$ ) and longitudinal ( $R_w$ ) radii of curvature.

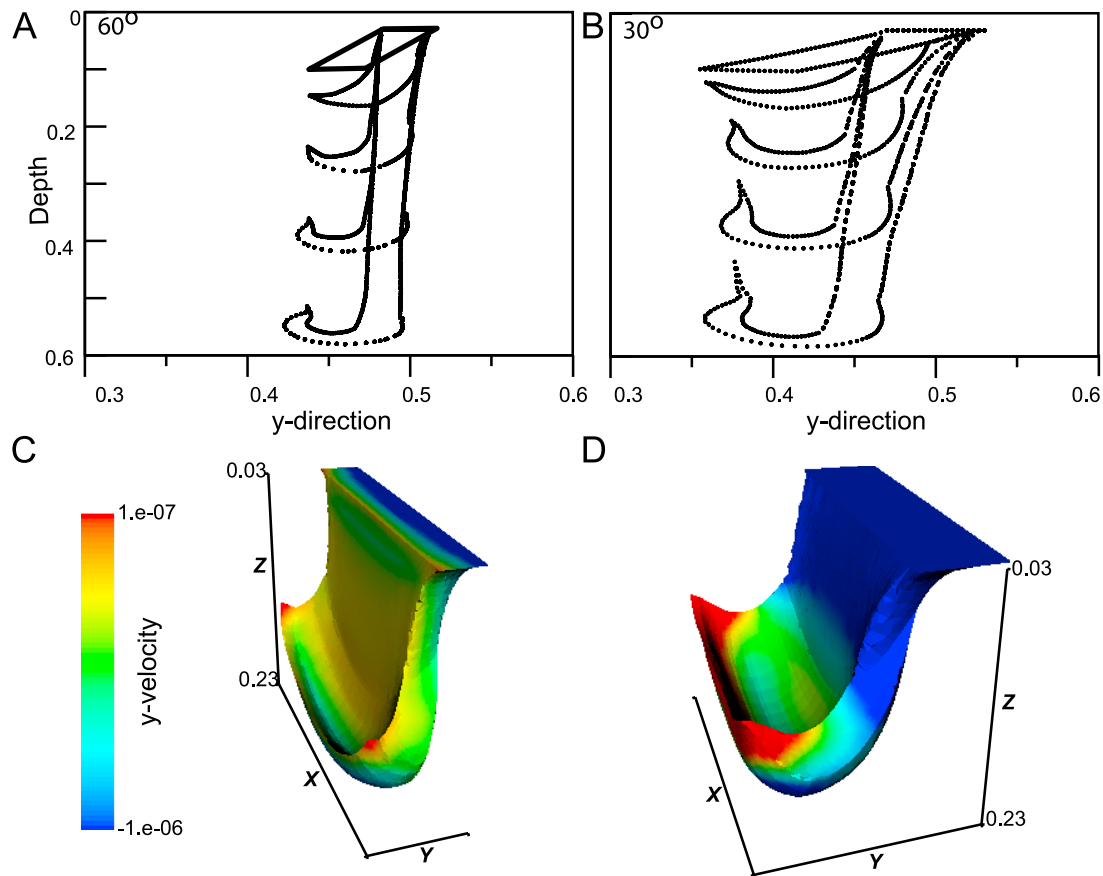


**Figure 5.** Geometry of the plate when subducted with an initial slab dip  $\alpha$ : (a and c)  $\alpha = 60^\circ$  and (b and d)  $\alpha = 30^\circ$ . Figures 5a and 5b show across-strike profiles, regularly sampled in time ( $n = 20$ ), and Figures 5c and 5d give a 3D view of the plate geometry when it reaches  $\sim 660$  km depth. The  $y$ -velocity on the surface of the plate is color-coded.

sider a  $90^\circ$  dip angle (or vertical slab), as set up in the reference model.

### 3.4. Slab to Mantle Viscosity Ratio

[16] We test different viscosity ratios (from  $10^{-2}$  to  $10^2$ ) between the lithosphere slab and the surrounding mantle (Figure 6a). Note that in the absence of any viscosity difference between the slab and mantle, the flow is that of a *Stokes* sinker. Furthermore, because we neglect the potential and highly unknown dependence of mantle and lithospheric rock viscosity on pressure, temperature or stress, our viscosities must be considered as effective values. Expanding the work of *Olson and Singer* [1985] on creeping, rising plumes, we identify three classes of jellyfishes based on the development of the jellyfish head: (i) Cavity jellyfishes, for which the plate viscosity is lower than that of the mantle; they feature well rounded heads connected to tails upon which tentacles are retracted (Figure 6a,  $\mu_s = 10^{-2}$ ). (ii) Diapiric jellyfishes develop when the system is isoviscous or close to it. They differ from

cavity jellyfishes by their well-individualized tentacles and even better rounded head (Figure 6a,  $\mu_s = 1$ ). (iii) Anvil jellyfishes develop when the viscosity ratio is much larger than 1. In this case, the slab grows into an inverted anvil-shaped cap (i.e., jellyfish head) along its leading edge (Figure 6a,  $\mu_s = 10^1$ – $10^2$ ). Because slab viscosity is higher than that of the surrounding mantle, anvil jellyfishes more likely apply to the Earth better than the other classes and in the following, we focus on this class. The deformation highly depends on the viscosity ratio, as illustrated by the strain rates along the vertical  $z$ -axis of the jellyfish (Figure 6b). The lower the viscosity ratio is, the higher the strain rates are, but they are always extensional in the tail and compressional in the head. Obviously, when  $\mu_s \gg 100$ , the slab does not deform and the head and tail do not develop.

[17] For high viscosity contrast, the radius of curvature  $R_w$  also decreases through time until it reaches a minimum value (Figure 6c). This indicates that, regardless of the viscosity ratio, the plate will tend toward an optimal shape (for an infinite domain

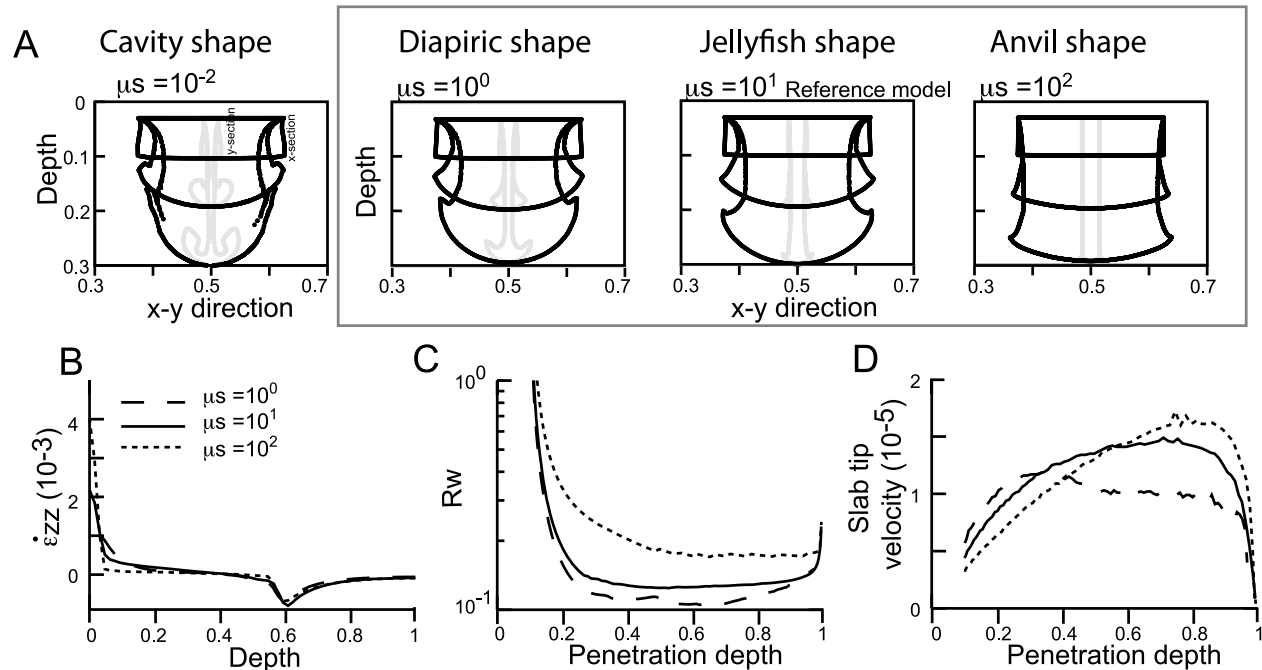


**Figure 6.** (a) Cross sections at selected depths along-strike (black) and across-strike (gray) and classification as function of the plate to upper mantle viscosity ratio  $\mu_s$  (see Table 1). Framed profiles are a selection of geologically plausible scenarios. (b) Vertical strain rate  $\dot{\epsilon}_{zz}$  profile along the central axis of the plate ( $x = 0.5$  and  $y = 0.5$ ). (c) Radius of curvature of the jellyfish head  $R_w$  as a function of maximum penetration depth and  $\mu_s$ . (d) Velocity of the plate head as a function of plate depth and  $\mu_s$ .

in the vertical direction), although this might require a very long descent time for a very large viscosity ratio. In all cases, the velocity increases gradually during the early evolutionary stages of the jellyfish at shallow depths; it reaches a maximum value, and eventually decreases when plate penetration is hindered by the undeformable bottom of the model experiment (Figure 6d).

[18] Interestingly, the viscosity ratio affects the sinking velocity. The slab penetrates faster into the mantle when  $\mu_s$  is high ( $\mu_s = 100$ ) and the velocity reaches its maximum value at greater depths than for less viscous slabs. When the viscosity ratio is low ( $\mu_s = 1$ ), the velocity starts to decrease at rather shallow depths ( $\sim 0.35$ ). These results can be explained by the joint effects of (i) the plate bulk mass (because the high viscous plate remained relatively undeformed, the boundary flux condition near the surface imposes a larger mass flux and thus larger negative buoyancy), (ii) plate stretching in the tail (which for low viscosity slabs, favors viscous dissipation in the surrounding mantle and prevents efficient stress transmission) and (iii) the passive resistance of the bottom of the mantle. Note that these results apparently differ from the solution obtained by *Hadamard* [1911] and *Rybczynski* [1911]

which predicts that the sinking velocity should decrease as the viscosity contrast increases. This is actually not very surprising because the latter solution only applies to a constant volume, deforming spherical bubble characterized by a lower viscosity than the surrounding fluid.

[19] Both extensive and compressive strain rates are larger in the tails and in the heads of low viscosity jellyfishes than of the high viscosity ones, implying that the sinking velocity of low viscosity slabs tends more rapidly to the *Stokes* velocity of the jellyfish head; this velocity yet remains lower than the sinking velocity of highly viscous slabs that are more negatively buoyant simply because of the larger resulting plate volume.

### 3.5. Viscosity Stratification Between Upper Mantle and Lower Mantle

[20] Scaled analog experiments of the subduction process [*Funiciello et al.*, 2003; *Griffiths et al.*, 1995; *Guillou-Frottier et al.*, 1995; *Kincaid and Olson*, 1987; *Schellart*, 2004] and numerical studies of subduction systems [*Behoukova and Čížková*, 2008; *Christensen*, 1996; *Čížková et al.*, 2007; *Davies*, 1995; *Enns et al.*, 2005; *Gaherty*

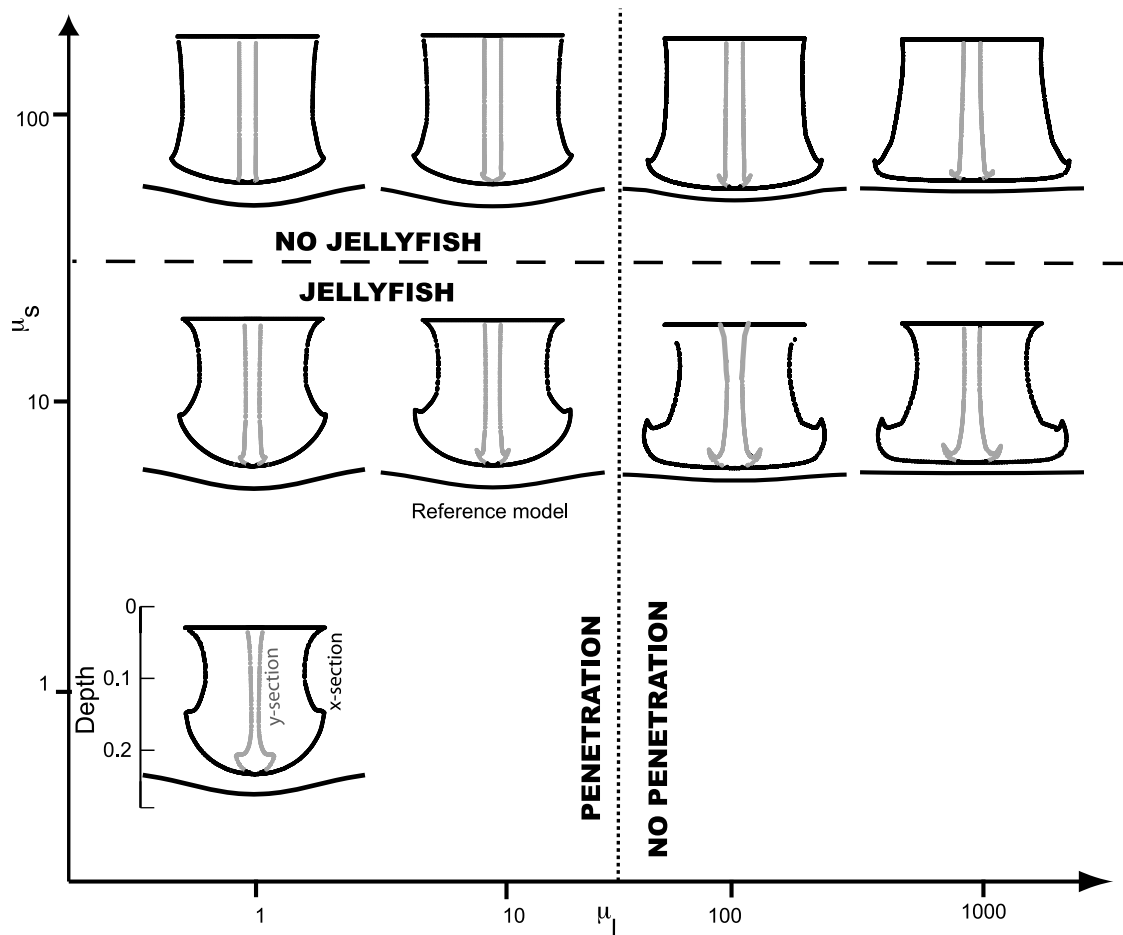


**Figure 7.** Different cases of slab geometry and slab penetration at the interface between the upper and lower mantle. Along-strike (black) and across-strike (gray) sections of the slab, as a function of the slab to upper mantle viscosity ratio  $\mu_s$  and the lower mantle to upper mantle viscosity ratio  $\mu_1$ . Solid black lines show the upper/lower mantle boundary.

and Hager, 1994; Goes et al., 2008; Houseman and Gubbins, 1997; Schellart et al., 2007; Tackley, 1993; Tao and O’Connell, 1993; Yoshioka and Wortel, 1995; Zhong and Gurnis, 1995] have already illustrated the modes of deformation of a stiff subducted slab reaching a fluid interface characterized by a viscosity and/or density increase. These studies have shown the importance of the density contrast [Christensen and Yuen, 1984] and viscosity ratio [Káráson, 2002; Kincaid and Olson, 1987] in governing whether the slab will lie along the interface, sink through it, or buckle and pile up at the interface [Ribe, 2003]. Here, we study the evolution of the jellyfish shape (i.e., low viscous slab) when the slab meets the 660 km boundary, which we either define as a viscosity or density contrast between the upper and lower mantle.

[21] Figure 7 summarizes the behavior of the plate as it forms a jellyfish shape and/or penetrates into the lower mantle as a function of  $\mu_s$ , the viscosity ratio

between the slab and the upper mantle, and  $\mu_1$ , the viscosity ratio between the lower and upper mantle.

[22] We observe a range of subducting plate shapes, with or without stratification boundary penetration, an indication that several factors are involved in the style of slab deformation when a fluid interface is present. We can define four different cases:

[23] (a) Jellyfishing (i.e., formation of a jellyfish shape) and penetration ( $\mu_s < 100$  and  $\mu_1 < 100$ ). The plate has a sufficiently low viscosity to transform into a jellyfish. The jellyfish head radius of curvature  $R_w$  is low (Figure 8a). The stratification is weak enough to permit the slab to sink into the lower mantle with minor deformation of the mantle stratification discontinuity. The plate continues to sink with a velocity decrease but without any interruption (Figure 8b). The interface deflects around the slab to form a blob and slowly collapses at the plate sinking velocity.

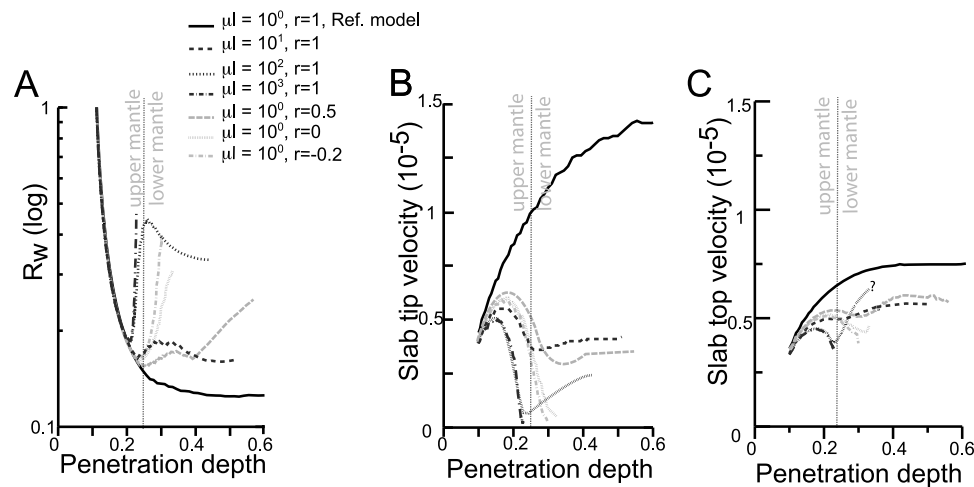


**Figure 8.** (a) Radius of curvature  $R_w$ , (b) velocity of slab tip, and (c) velocity of slab top measured as a function of the maximum plate penetration depth for different lower to upper mantle viscosity ratio  $\mu_l$  (black), and density indices  $r$  (see text). The slab to upper mantle viscosity ratio  $\mu_s$  is set to 10.

[24] (b) Jellyfishing and no penetration ( $\mu_s < 100$  and  $\mu_l > 100$ ). The plate transforms into jellyfish but does not penetrate the lower mantle. The plate stops close to the stratification boundary and the jellyfish head flattens. This case is also characterized by a rapid increase in  $R_w$  when the plate reaches the interface, followed by a phase of decreasing  $R_w$  (Figure 8a).

[25] (c) No jellyfishing and penetration ( $\mu_s > 100$  and  $\mu_l < 100$ ). The plate is too viscous and cannot evolve toward a jellyfish shape before it reaches the upper/lower mantle boundary but crosses it because the viscosity ratio  $\mu_l$  is low enough. Consequently, the deflected interface collapses around the quasi-rigid slab. The viscosity ratio between the plate and the fluid decreases in the lower mantle allowing plate thickening in the lower fluid.

[26] (d) No jellyfishing and no penetration ( $\mu_s > 100$  and  $\mu_l > 100$ ). The plate does not cross the stratification boundary and keeps a slab shape because the viscosity ratio with the surrounding mantle is too high. Furthermore the strong viscosity contrast with lower mantle does not permit slab deformation and slab penetration. The interface stays straight.

[27] Our results therefore demonstrate that the penetration of the plate into the lower mantle mainly depends on mantle stratification while the widening of the slab tip and jellyfish formation mostly depends on the slab strength (i.e., viscosity ratio between the subducting plate and the surrounding mantle).

[28] Note that all slabs should ultimately penetrate if given sufficient time. Here, we define penetration

mode when the characteristic slab sinking velocity is comparable to the characteristic penetration velocity, i.e., the slab does not pile up on the upper mantle/lower mantle interface.

### 3.6. Density Stratification Between Upper and Lower Mantle

[29] To investigate the influence of the various density contrasts between the sinking slab, upper mantle and lower mantle, we used the critical dimensionless parameter  $r$  defined by *Kincaid and Olson* [1987] (Figure 9) in which the slab/lower mantle density contrast is normalized by the slab/upper mantle density contrast:  $r = (\rho_s - \rho_{lm})/(\rho_s - \rho_{um})$ .  $r = 1$  corresponds to a uniformly dense fluid (no density contrast between the upper and lower mantle), while negative values of  $r$  correspond to a denser lower mantle than the sinking slab. Results are given for  $-0.2 < r < 1.0$  (Figures 8 and 9). We identify four cases in Figure 9:

[30] In Figure 9a,  $r = -0.2$ , which indicates strong stratification and no slab penetration. While the slab sinks through the upper mantle and reaches the discontinuity, its deformation is controlled by the viscosity ratio between the slab and the upper mantle. The leading edge thickens when it meets the undeformable interface.  $R_w$  increases and the sinking velocity decreases (Figures 8a and 8b).

[31] In Figure 9b,  $r \sim 0$ , which indicates partial slab penetration into the lower mantle. Sinking rates are lower than when  $r = -0.2$ .  $R_w$  increases (Figures 8a and 8b) when the slab reaches the mantle discontinuity. The leading edge of the slab reclines onto the

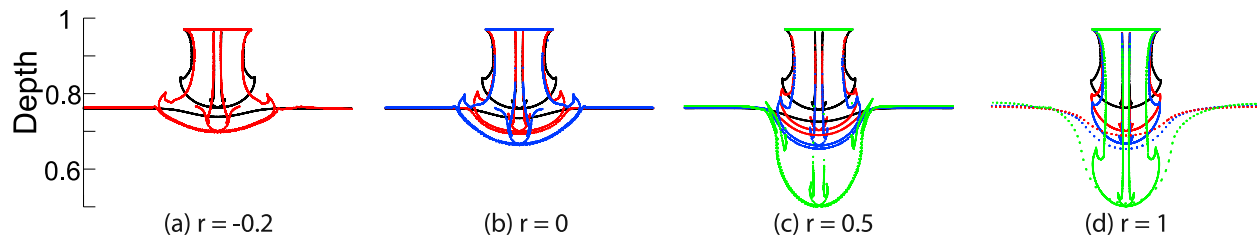


**Figure 9.** Cross-strike and along-strike sections of the entire plate at four selected depths (0.24, black, 0.3 red, 0.34 blue and 0.5 green) for different values of the density parameter  $r$  (see text). The upper/lower mantle boundary is indicated by horizontal lines. Note some selected depths at  $r = -0.2$  and  $r = 0$  are missing when the plate does not cross the upper/lower mantle boundary.

interface. Buoyancy forces in the lower mantle are not strong enough to stall subduction until the slab has penetrated below the discontinuity (around 1/10 penetration in the lower mantle). Within this range of density contrasts the initial penetration is however always limited.

[32] In Figure 9c,  $r \sim 0.5$ , which indicates slab penetration. The slab sinks through the lower layer but only on a very long time scale because the sinking velocity decreases (Figure 8b). The deflected interface collapses around the slab into a blob. Both the slab and the deformed interface descend slowly.

[33] In Figure 9d,  $r > 0.5$ , which indicates weak stratification. The stratification is weak enough to permit the slab to sink into the lower mantle with only minor deformation of the interface. The slab acquires the jellyfish form as described in the above section. Both the viscosity and density stratification of the mantle intensify the decrease in slab sinking rates at its deep head, but also at the surface level (Figure 8c).

#### 4. Comparison to the Real Earth

[34] Several types of seismically derived data address the problem of slab deformation within the mantle, as reviewed by Lay [1994]. The quasi-planar geometry of subducting slabs in the upper mantle was first defined from the distribution of large earthquakes along Wadati-Benioff zones [Isacks and Barazangi, 1977; Jarrard, 1986]. In addition, maps of earthquake focal positions [Engdahl et al., 1998] provided high resolution three dimensional images of the seismogenic regions surrounding subduction zones that gave rise to general geometric and deformation models of mantle slabs, such as the RUM model [Gudmundsson and Sambridge, 1998]. Furthermore, global seismic tomography models [Bijwaard et al., 1998; Ding and Grand, 1994; Fukao, 1992; Grand, 1994; van der Hilst, 1995;

van der Hilst and Widiyantoro, 1997; Wortel and Spakman, 2000; Becker and Boschi, 2002] provide more insights into slab morphology, including those characterized by a relatively low seismicity [Li et al., 2008], as well as the distribution of seismic velocity anomalies in the mantle surrounding the slabs. Most recently, seismic images have been interpreted in terms of the most probable density field yielding the observed seismic velocity anomalies, which in turn have been used to derive models of self-consistent mantle flow [e.g., Becker, 2006; Conrad et al., 2007; Conrad and Husson, 2009; Mitrovica and Forte, 2004; Moucha et al., 2007].

[35] All above mentioned methods are complementary and show that subducting slabs are significant structures in the upper mantle, that the majority of them penetrates into the lower mantle and that they are characterized by a rather complex three-dimensional deformation pattern (rather than being planar slabs) [Yamaoka et al., 1986]. In many instances, which we will describe below, tomographic images suggest a characteristic shape for the slab, with a relatively narrow trace in the upper mantle and a wider anomaly in the mid-lower mantle [Kárason and Van der Hilst, 2001]. Clearly, subducted lithosphere is rarely imaged as a slab-shaped feature but rather as a spheroidal anomaly. As shown by Kárason [2002], using paleogeographic reconstructions, geophysical observations are therefore consistent with our theoretical prediction that subducted slabs should deform as they penetrate into the mantle to take the shape of a jellyfish. The distribution of focal mechanisms shows that stresses within the subducted slab are characterized by downdip extension in its upper part (between 100 and 300 km depth), which is also associated with the narrow section of the slab, and by downdip compression in the deeper part of the slab, i.e., toward the 660 km boundary [Apperson and Frohlich, 1987; Isacks and Molnar, 1969; Vassiliou et al., 1984], which is associated with the thickest section of the

**Table 2.** Geometrical Classification of Slabs and Subduction Parameters

Category	Name <sup>a</sup>	V <sub>s</sub> <sup>b</sup> (mm/a)	Age <sup>c</sup> (My)	Φ <sup>d</sup> (km)
Type 1	N-Kuril	77.99	110	8591
	Central America	62.27	17.6	1089.26
	Alaska W	59.4	52	3091.92
	Alaska E	50.2	41.8	2128.45
	Peru	61.1	28.8	1756.51
	Java-Sumatra	47.39	69.93	3356.64
Type 2	Hellenic	42	100	5100
	North-central Chile	68.13	52.12	3542.07
	S-Kuril	75	120.4	9042.04
	Japan	89.75	129.5	11661.47
Type 3	Izu-Bonin	50	138.25	6943.23
	Tonga	157.25	107.25	17754.16
	Mariana	40.11	151.61	6143.23
Type 4	Kermadec	55	99	5464.8
	Scotia	40	38.16	1525.63
	Aleutian	53.21	56.23	2945.32
	Caribbean	8	96.66	788.23
	North America	31	9.4	292.90
	South Chile	70	33.8	2376.47
	Ryuku	85.8	44.2	3777.33
	Calabria	50	80	4160

<sup>a</sup>Trench segmentation is based on *Gudmundsson and Sambridge* [1998].

<sup>b</sup>V<sub>s</sub> = V<sub>sub</sub> - V<sub>t</sub>, where V<sub>s</sub> is the average subduction velocity along the subduction zone segments, V<sub>sub</sub> is the velocity of the subducting plate and V<sub>t</sub> is the trench migration velocity (from the compilation of *Heuret and Lallemand* [2005]). The classification of slab deformation is based on the shape of the Wadati-Benioff zone inferred from deep seismicity [*Engdahl et al.*, 1998] and the results of the seismic tomography model of *Li et al.* [2008].

<sup>c</sup>Mean subduction age along the trench segments [from *Heuret and Lallemand*, 2005; after *Müller et al.*, 1997].

<sup>d</sup>Φ: Slab thermal parameter (age \* V<sub>s</sub>).

slab. Such a distribution of stress, and thus strain rate, along the subducting plate is identical to that predicted in our models of a slab transforming into a jellyfish (Figure 3c).

[36] By conducting a careful review of high resolution images of Wadati-Benioff zones derived from the accurate localization of seismicity [*Engdahl et al.*, 1998] and tomographic images obtained from P waves seismic travel time anomalies [*Li et al.*, 2008], we came to the conclusion that there are four main categories of slabs (defined in Table 2) in the Earth's mantle, varying in their shape (on whether subducted slabs thicken at depth or not) and interaction characteristics at/with the 660 km discontinuity (whether subducted slabs penetrate or not in the lower mantle). To illustrate these categories, we explored the structure of a variety of subduction systems and slab geometries in 2D and 3D views derived from a P wave seismic tomography model [*Li et al.*, 2008]. We selected well-defined examples that illustrate each category (Figure 10). These categories are:

[37] Type 1 is penetration and thickening (the Hellenic slab) (Figures 10a, 10e, 10i, and 10m). The subducted lithosphere crosses the 660 km boundary with a small perturbation in thickness, which increases in the mid-lower mantle. Below 660 km, a fast velocity anomaly appears in the subducting plate which widens to ~400 km in the mid-mantle (~1200 km depth). The penetration of the subducted slab through the 660 km discontinuity and slab thickening in the mid-mantle (~1200 km) are the two remarkable features that are observed in other tomographic studies of this region [*Piomallo and Morelli*, 2003; *Spakman et al.*, 1993]. Other subduction zones where comparable features are observed include Central America, N-Kuril [*Ding and Grand*, 1994], Java [*Fukao*, 1992; *Puspito et al.*, 1993; *Widiyantoro and van der Hilst*, 1996] and India-Tibet [*Bijwaard et al.*, 1998; *Grand et al.*, 1997].

[38] Type 2 is slab deflection with little or no penetration (the Izu-Bonin slab). In this category, slabs are significantly deflected above the 660 km discontinuity to form a sub-horizontal high seismic velocity zone. Vertical cross section in this area (Figures 10b, 10f, 10j, and 10n) clearly demonstrates that the slab has been strongly deflected at the 660 km discontinuity with only a slight hint that it may have penetrated in the lower mantle. The slabs in the Izu-Bonin [*Tajima and Grand*, 1998], in S-Kuril [*Tajima and Grand*, 1995] and Japan subduction systems are the best examples of this category.

[39] Type 3 is pure penetration (the Mariana slab). As shown in Figures 10c, 10g, 10k, and 10o and as seen in many tomographic studies [e.g., *Fukao*, 1992; *van der Hilst and Seno*, 1993; *Zhou*, 1988], the Mariana slab appears to penetrate the 660 km discontinuity to reach the mid-mantle without significant thickening. Another typical example is the Kermadec slab [*Zhao et al.*, 1997].

[40] Type 4 is no penetration and no thickening (the Scotia slab). This category includes the Calabria, Aleutian, Caribbean, Ryukyu and the Scotia slabs that do not penetrate into the lower mantle and do not seem to experience any thickening at their base (Figures 10d, 10h, 10l, and 10p). However, many slabs of this type may lay flat on the 660 km discontinuity because of slab rollback (e.g., Calabria or Scotia), which makes the comparison to our experiments more uncertain.

[41] In order to further characterize the shape of the subducting slabs, we mapped data from the tomographic model of *Li et al.* [2008] on a Cartesian grid using the *GMT* software [*Wessel and Smith*, 1991] to

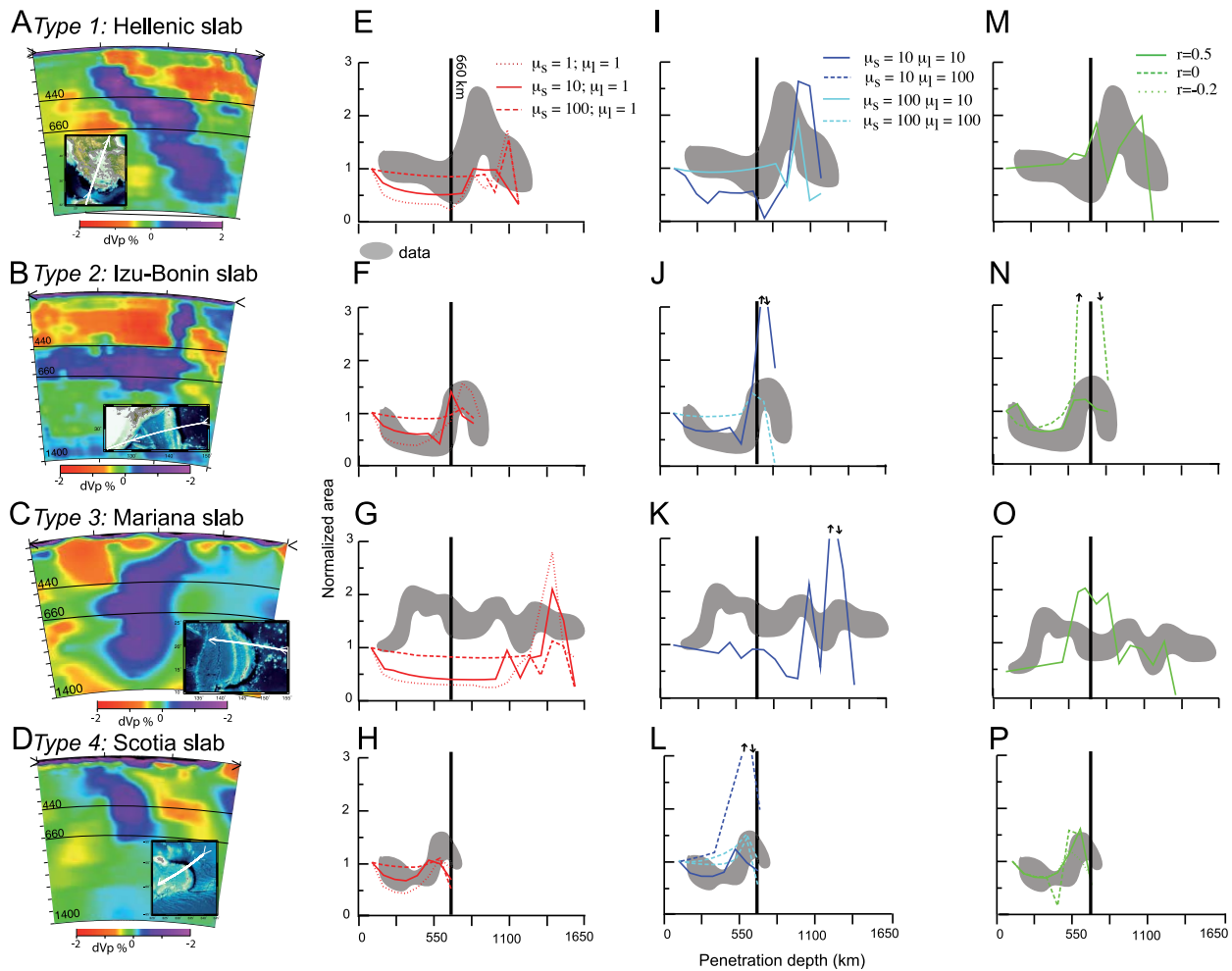


**Figure 10.** (a–d) Vertical profiles across seismic tomography model of *Li et al.* [2008] (global P wave model) and (e–p) slab thickening illustrated by the evolution of the predicted sectional area (by numerical models, color curves) and sectional area inferred from geophysical data (gray areas) as a function of maximum penetration depth. This is shown for ranges of slab to upper mantle viscosity ratio (red curves, Figures 10e–10h), lower to upper mantle viscosity ratio (blue curves, Figures 10i–10l), and density contrast between the slab and the lower mantle (green curves, Figures 10m–10p), for the Hellenic (Figures 10a, 10e, 10i, and 10m), Izu-Bonin (Figures 10b, 10f, 10j, and 10n), Mariana (Figures 10c, 10g, 10k, and 10o) and Scotia (Figures 10d, 10h, 10l, and 10p) subduction zones which are type 1, 2, 3 and 4 respectively. It is only for visualization/illustration purpose that the vertical sections of seismic tomography models are provided, and the comparison remains qualitative.

compute horizontal cross-sections at 100 km intervals of the seismic velocity anomalies from which we estimated the surface area of the slabs as they penetrate into the mantle, from 100 to 1400 km depths. In that way, we optimize the accuracy of estimates of the slab thinning/thickening with depth. In fact, at each depth, we considered three contours of the velocity anomaly contrast (minimum, mean and maximum relative velocities) to avoid artifacts arising from the inherent resolution of tomographic models. Note that no unique values for the seismic velocity contrasts can be selected for they vary with depth, in particular because of the thermal relaxation of the slabs during their downward route; contouring

is therefore arbitrary and to some extent, subjective. We normalized the surface areas comprised inside each of the contours by the contour area at the surface to obtain dimensionless vertical profiles of the slab thickness (extracted from horizontal section). This procedure was also performed on some of our numerical model results (Figure 10).

[42] These values for slab thickness as they penetrate in the mantle are more relevant qualitatively than quantitatively. Although *Li et al.* [2008] suggest that the deep mantle parts of the slab structures are well resolved and are not affected by artifacts arising from the uneven distribution of seismic sources and

receivers, which suggest some robustness, we emphasize that the comparison of experiments to real Earth should be taken with care.

[43] For each of the four slab categories, we compared thickness profiles from the tomographic model to those obtained from numerical models in which we varied the viscosity ratio  $\mu_s$  between 1 and 100, the viscosity ratio  $\mu_1$  between 1 and 1000 and the density parameter  $r$  between  $-0.2$  and 1 (Figure 10). To facilitate the comparison between data and models, we show model-predicted surface area profiles for model times that best correspond to subduction/penetration level suggested by each of the four tomographic images. The tentacles from the predicted model as described in results part are not considered (i.e., we include tentacles in surface area calculations) because the resolution of seismic tomography models is not sufficient to characterize their geometry.

[44] We first notice that, in both the numerical models, where the viscosity mantle stratification ( $\mu_1 > 1$ ) or the density mantle stratification ( $r < 1$ ) impacts on plate penetration and on its deformation, and in some of the tomographic images, the formation of the jellyfish head and the corresponding thickening of the slab usually occurs deeper than the imposed viscosity/density jump at 660 km depth. This implies that, in some cases the discontinuity impacts the thickening of the subducting slab, the formation of the jellyfish may take place at greater depths and is thus likely to result from an independent process, as advocated by our numerical model results.

[45] Then, in the first two categories, slab thickening occurs at (i.e., type 2, Izu Bonin slab, Figures 10b, 10f, 10j, and 10n) or below the 660 km discontinuity (i.e., type 1, Hellenic slab, Figures 10a, 10e, 10i, and 10m); comparing tomographic models and the results of the numerical models suggests that the formation of the jellyfish head is best explained either by a low increase in viscosity from upper to lower mantle ( $\mu_1 \sim 10$ ), consistent with previous studies based on the interpretation of the geoid [Moresi and Gurnis, 1996] or by a weak jump in density between the upper and lower mantle ( $r \sim 0.5$ ), as suggested by other model results [Christensen and Yuen, 1984]. In nature, we found it impossible to discriminate the two causes; a combination of both is probably responsible for slab thickening. The observed surface area versus depth profiles are best explained with a relatively low slab viscosity (only  $\sim 10$ – $100$  times the mantle viscosity), which confirms the results of Loiselet *et al.* [2009].

[46] In the third category, the Mariana slab displays a rather different behavior that suggests that the slab may be stronger than slabs belonging to type 1, and does not evolve into a jellyfish shape as it descends through the upper mantle. The slight thickening that appears in the slab cross-sectional area observed at depths between 1100 and 1650 km may be due to the relatively poor resolution of the tomographic images at those depths or to a mild density or viscosity stratification as suggested by Čížková *et al.* [1996], Hager and Richards [1989], and Lambeck and Johnston [1998].

[47] In the fourth category, thickening of the Scotia slab as it approaches the 660 km discontinuity could be explained by the formation of a jellyfish head, which in turns requires a relatively low viscosity/strength subducting plate.

[48] In order to evaluate the relationship between the geometries derived from the analysis of a tomographic model, and the factors that might control it such as the density and/or viscosity of subducted slabs, we use the parameter  $\Phi$ , introduced by Wortel and Vlaar [1988], defined as  $\Phi = \text{age} * V_s$  (where *age* is the average age of lithosphere at the time of subduction and  $V_s$  is the average velocity of subduction along trench segments) (see Table 2). This parameter can be interpreted as a proxy for the thermal maturation of the slab, which affects both the viscosity and density of the slab. There is a clear distribution of slab categories (type 1, 2, 3 or 4) as a function of  $\Phi$  (Figure 11): (i) slabs with small thermal parameters  $\Phi$  (or hot slabs) more easily jellyfish (i.e., type 1) than those with larger values for  $\Phi$  (i.e., type 3); and (ii) slabs with large values of  $\Phi$  tend to subduct more easily for they are presumably stiffer and denser. For very small thermal parameters, thermal diffusion may have had enough time to heat up the slabs so that they do not show up in seismic tomography. Alternatively, heated slabs may have lost their initial negative buoyancy and are no longer able to continue to subduct to greater depths than the transition zone (type 4, Calabria, Scotia slabs). Last, slabs of type 2 seem to be at odds with our previous analysis, for they appear to pond on the 660 km discontinuity, whereas in our models stiff slabs are predicted to penetrate into the lower mantle and not to deform. The departure between our models and the predictions given by the thermal parameter  $\Phi$  may however reflect the fact that this proxy does not apply for slabs of type 2 (Izu-Bonin, S-Kuril, Japan and Tonga slabs).

[49] In our numerical models, and thus in our interpretation of the various slab geometries suggested by

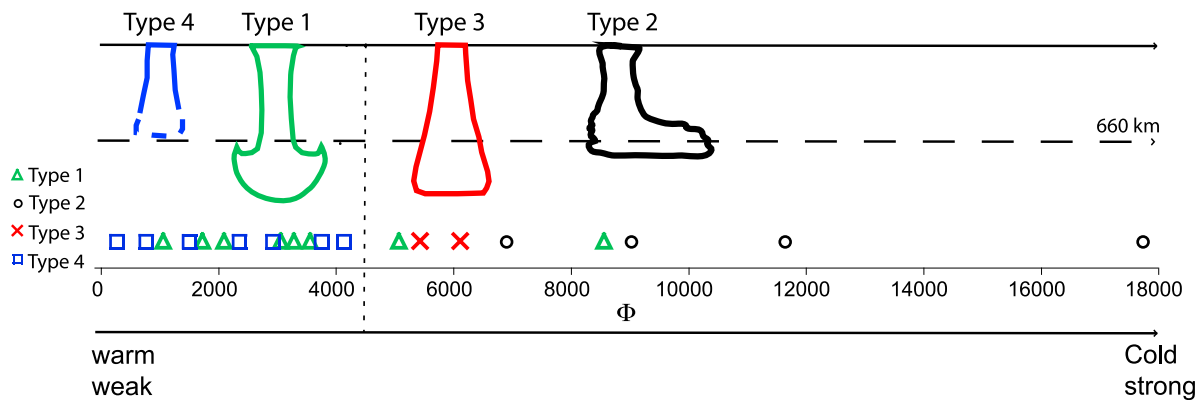


**Figure 11.** Geometrical classification of slabs (types 1 (green), 2 (black), 3 (red) and 4 (blue), see text) and correlation to the thermal parameter  $\phi$  [Wortel and Vlaar, 1988].  $\Phi$  is the product of the average age of lithosphere and of the subduction rate (age \* Vs) along the trench segment (defined from Gudmundsson and Sambridge [1998]).

tomographic models, we have assumed that slab motion is primarily driven by its buoyancy, i.e., the main force acting on the subducting oceanic lithosphere is the gravitational force arising from the high density of the plate with respect to the surrounding mantle. This has led us to interpret the observed thickening of weak slabs in the vicinity of the 660 km discontinuity as resulting from the formation of a jellyfish head in response to viscous drag between the slab and the mantle, potentially enhanced by the presence of a viscosity and/or density contrast between the upper and lower mantle. The former process (jellyfishing), in turn implies that the viscosity ratio between the slab and the mantle is relatively small (order 10), in other words that slabs are relatively weak. The latter process (interaction with the 660 km discontinuity) is supported by the compressive nature of the focal mechanisms of deep earthquakes [Sacks and Molnar, 1969], which clearly indicates the presence of resisting forces deeper than the transition zone, resulting from an increase in viscosity or a decrease in the density contrast between the slab and the surrounding mantle, and thus a decrease in the driving force.

[50] However, another explanation for the thickening of the slab along the 660 km discontinuity relies on the subduction (or penetration) velocity being imposed to the slab by other forces, either originating at the mid-ocean ridge (i.e., ridge push) or along other segments of the subducting lithosphere. If this is true and the trench migration velocity is significantly higher than the penetration velocity of the slab in the lower mantle (due to resistance force), slabs will have to deform on the 660 km discontinuity, to flatten and lie horizontally on it [Christensen, 1996; Enns et al., 2005; Griffiths et al., 1995; Guillou-

Frotier et al., 1995; Olbertz et al., 1997; Tagawa et al., 2007]. This scenario may explain why the Izu-Bonin slab flattens on the 660 km discontinuity [van der Hilst and Seno, 1993] whereas the Mariana slab penetrates it; similarly, the change in the style of subduction from the northern to southern Kuril [Ding and Grand, 1994; Fukao, 1992] is a potential illustration.

## 5. Discussion

[51] Seismic tomography images provide evidence for a strong deformation of some sections of the subducted lithosphere in the Earth's mantle. In the deep Earth's interior, some slabs may flatten and pond above or within the transition zone, such as beneath the Chilean Andes, the Aleutian, the S-Kuril, Japan, and Izu-Bonin. Other slabs tend to be deflected and lie sub-horizontally on the upper to lower mantle transition region before (at least for some of them) penetrating into the mid-lower mantle (such as in the N-Kuril, Hellenic, and the Philippines subduction systems), or well into the lower mantle (such as beneath the Peruvian Andes, Java, Mariana and Kermadec). In the latter case, slabs narrow in the upper mantle and anomalously thicken in the mid-lower mantle. Some authors explain this feature as resulting from a buckling instability [Griffiths and Turner, 1988; Ribe et al., 2007]. Alternatively, Christensen and Yuen [1984] and Káráson [2002] showed that the large mid-mantle seismic anomaly could either be explained by geochemical and mineralogical changes in the slab as a function of depth or by the presence of a substantial viscosity jump at the 660 km discontinuity that modulates the penetration of an isoviscous plate.

[52] Here we propose, on the basis of the results of a large number of numerical experiments and their comparison to tomographic images, that the deformation of the subducting lithosphere mainly results from the interaction of a relatively weak slab with the surrounding viscous mantle, leading to the deformation of the planar lithosphere into a jellyfish.

[53] For each of the four subduction categories considered here, the comparison with model scenarios suggests that the viscosity ratios between the slab and the upper mantle ranges between 10 and 100. This is in accordance with *Husson* [2006] who found a good agreement between the topography observed above subduction zones and the dynamic topography computed assuming isoviscous flow in the mantle. *Čížková et al.* [2002] also found that slabs must be relatively weak in order to be deflected in the transition zone. Based on the results of analog experiments, [*Funiciello et al.*, 2008; *Schellart*, 2009] suggested that the observed trench and plate velocities and slab bending respectively are indicative of relatively weak slabs. More comprehensive reviews are given by *Billen* [2008] and *Becker and Faccenna* [2009].

[54] The low slab strength we predict here is at odds with the setup of many other analog and numerical models [*Capitanio et al.*, 2007; *Clark et al.*, 2008; *Conrad and Hager*, 1999; *Funiciello et al.*, 2003; *Morra et al.*, 2006; *Royden and Husson*, 2006; *Schellart*, 2004; *Stegman et al.*, 2006; *Zhong and Gurnis*, 1994] where the viscosity ratio between the subducted lithosphere and the surrounding mantle is set between  $10^2$  and  $10^5$ . Although rock strength experiments also predict stiffer slabs than suggested here [see, e.g., *Kohlstedt et al.*, 1995], our predicted range of viscosity ratios is in accordance with global models [*Zhong and Davies*, 1999] that suggest that slabs should be 100 times more viscous than the upper mantle in order to fit geoid and dynamic topography data. *Loiselet et al.* [2009] independently suggest that the longitudinal curvature of slabs can only be achieved if the slab to mantle viscosity ratio is at most  $10^2$ .

[55] In summary, any model that predicts a significant thickening of slabs descending in the upper mantle requires a weak subducted lithosphere, i.e., at most two orders of magnitude stiffer than the upper mantle. Higher than that, slabs are too strong to deform at the length-scale of the upper mantle. This result in turn indicates that slabs have limited time to acquire a characteristic jellyfish shape. Our interpretation of the seismically inferred thickening of

slabs in the upper mantle applies well to young subduction zones, such as Scotia. In contrast, *Loubet et al.* [2009] have interpreted the apparent thickening of slabs in older, longer-lasting subduction zones as resulting from the periodic buckling of a relatively weak slab at the 660 km discontinuity by simple accumulation of subducting material.

[56] The comparison between our model predictions and seismic tomography data also suggests that the subducting plate should slow down and pond at the 660 km discontinuity if a viscosity or density contrast exists between upper and lower mantle, as already proposed by for example *Enns et al.* [2005]. The apparent slab widening at depth suggests that the slab is indeed stronger than the mantle but unfortunately an accurate estimate of the viscosity contrast cannot be obtained independently of any density variation that might exist across the 660 km discontinuity.

[57] Once the jellyfish penetrates into the lower mantle, the velocity of the subducting plate appears to remain constant, seemingly in contradiction with *Zhong and Gurnis* [1995] and *Christensen* [1996] who predicted an acceleration of the slab after penetrating the 660 km discontinuity. The difference in interpretation may occur because in their models there are (i) phase transitions with a negative Clapeyron slope along the 660-km discontinuity that foster subduction, or, (ii) alternatively, because the trench is actively retreating, while in our models, slabs subduct vertically.

## 6. Conclusions

[58] We have investigated the behavior of a slab subducting in the Earth's mantle driven by its negative buoyancy. We have showed that a relatively weak plate (at most two orders of magnitude times stiffer than the surrounding mantle) will form a characteristic jellyfish shape as it falls through the mantle. This is the optimal shape that a deformable object falling in a viscous fluid will acquire, regardless of its original shape, in order to probably minimize the viscous dissipation in the fluid. The jellyfish consists of a wide head experiencing vertical shortening and a long tail experiencing vertical lengthening. This pattern of deformation is consistent with the observed distribution of down-dip extensional and compressional stresses along subducting slabs and with observed slab geometries at mid-mantle depths that are derived from tomographic images. This characteristic jellyfish shape

naturally evolves from that of a planar subducting plate, but the few other initial shapes that we tested numerically or in analog models also adopt similar behaviors and all tend to jellyfish shape. We have used a linear viscosity for both the slab and the mantle, which implies that strain rate and, subsequently, subduction velocity linearly scales with the imposed density contrast between the slab and the mantle. The value of the density contrast between the slab and the surrounding mantle thus does not influence the geometry of the subduction process nor the depth range over which the jellyfish head forms.

[59] The plate to mantle viscosity ratio is important to the deformation of the plate. Lithosphere strength is crucial physical parameter that controls the dynamics of subduction zone.

[60] By comparing model predictions with observations (inferred from seismic tomography and earthquake focal mechanism solutions) we therefore provide additional constrains on the viscosity contrast between subducting slabs and the surrounding mantle by suggesting that slabs are weak. The final jellyfish shape also depends on the initial slab width, or more precisely, its aspect ratio. Furthermore, in cases where the initial slab is not vertical, we have shown that the slab turns into an asymmetrical jellyfish. This “spoon” shape is consistent with many observed geometries (derived from seismic tomography and from the distribution of earthquakes in Wadati-Benioff zones); the Hellenic slab is one of the most striking examples of such spoon-shaped subducting slabs.

[61] Last, one way to reconcile the observation that some slabs are thickened around the 660 km discontinuity while others seem to thicken at mid- to lower mantle depths or deeper, is to consider (i) that the subducted plate is in general sufficiently weak to become a jellyfish during its fall in the upper mantle and (ii) that it meets at the 660 km depth a low viscosity and/or high density jump that lowers its sinking velocity.

## Acknowledgments

[62] This work was supported by the College doctoral de Bretagne (Université Européenne de Bretagne) (C.L.) and by a “Chaire d’Excellence Senior de l’ANR” (J.B.). We thank P. Fullsack for stimulating discussions. Suggestions by anonymous reviewers and by Editor Thorsten Becker helped to greatly improve this paper.

## References

- Apperson, K. D., and C. Frohlich (1987), The relationship between Wadati-Benioff zone geometry and P, T and B axes of intermediate and deep focus earthquakes, *J. Geophys. Res.*, *92*, 13,821–13,831.
- Becker, T. W. (2006), On the effect of temperature and strain-rate dependent viscosity on global mantle flow, net rotation, and plate-driving forces, *Geophys. J. Int.*, *167*, 943–957, doi:10.1111/j.1365-246X.2006.03172.x.
- Becker, T. W., and L. Boschi (2002), A comparison of tomographic and geodynamic mantle models, *Geochem. Geophys. Geosyst.*, *3*(1), 1003, doi:10.1029/2001GC000168.
- Becker, T. W., and C. Faccenna (2009), A review of the role of subduction dynamics for regional and global plate motions, in *Subduction Zone Geodynamics*, edited by S. Lallemand and F. Funiciello, pp. 3–34, doi:10.1007/978-3-540-87974-9\_1, Springer, Berlin.
- Behoukova, M., and H. Čížková (2008), Long-wavelength character of subducted slabs in the lower mantle, *Earth Planet. Sci. Lett.*, *275*, 43–53, doi:10.1016/j.epsl.2008.07.059.
- Bevis, M. (1986), The curvature of Wadati-Benioff zones and the torsional rigidity of subducting plates, *Nature*, *323*, 52–53, doi:10.1038/323052a0.
- Bijwaard, H., W. Spakman, and E. R. Engdahl (1998), Closing the gap between regional and global travel time tomography, *J. Geophys. Res.*, *103*(B12), 30,055–30,078.
- Billen, M. I. (2008), Modeling the dynamics of subducting slabs, *Annu. Rev. Earth Planet. Sci.*, *36*(1), 325–356, doi:10.1146/annurev.earth.36.031207.124129.
- Billen, M. I., and M. Gurnis (2005), Constraints on subducting plate strength within the Kermadec trench, *J. Geophys. Res.*, *110*, B05407, doi:10.1029/2004JB003308.
- Braun, J., C. Thieulot, P. Fullsack, M. DeKool, C. Beaumont, and R. Huismans (2008), DOUAR: A new three-dimensional creeping flow numerical model for the solution of geological problems, *Phys. Earth Planet. Inter.*, *171*(1–4), 76–91, doi:10.1016/j.pepi.2008.05.003.
- Capitanio, F. A., G. Morra, and S. Goes (2007), Dynamic models of downgoing plate-buoyancy driven subduction: Subduction motions and energy dissipation, *Earth Planet. Sci. Lett.*, *262*(1–2), 284–297, doi:10.1016/j.epsl.2007.07.039.
- Christensen, U. R. (1996), The influence of trench migration on slab penetration into the lower mantle, *Earth Planet. Sci. Lett.*, *140*, 27–39, doi:10.1016/0012-821X(96)00023-4.
- Christensen, U., and D. Yuen (1984), The interaction of a subducting lithosphere slab with a chemical or phase boundary, *J. Geophys. Res.*, *89*, 4389–4402, doi:10.1029/JB089iB06p04389.
- Čížková, H., O. Čadek, D. A. Yuen, and H. Zhou (1996), Slope of the geoid spectrum and constraints on mantle viscosity stratification, *Geophys. Res. Lett.*, *23*(21), 3063–3066, doi:10.1029/96GL02257.
- Čížková, H., J. van Hunen, A. P. van den Berg, and N. J. Vlaar (2002), The influence of rheological weakening and yield stress on the interaction of slabs with the 670 km discontinuity, *Earth Planet. Sci. Lett.*, *199*, 447–457, doi:10.1016/S0012-821X(02)00586-1.
- Čížková, H., J. van Hunen, and A. van den Berg (2007), Stress distribution within subducting slabs and their deformation in the transition zone, *Phys. Earth Planet. Inter.*, *161*(3–4), 202–214, doi:10.1016/j.pepi.2007.02.002.

- Clark, S. R., D. Stegman, and R. D. Muller (2008), Episodicity in back-arc tectonic regimes, *Phys. Earth Planet. Inter.*, *171*(1–4), 265–279, doi:10.1016/j.pepi.2008.04.012.
- Conrad, C. P., and B. H. Hager (1999), Effect of plate bending and fault strength at subduction zones on plate dynamics, *J. Geophys. Res.*, *104*, 17,551–17,571, doi:10.1029/1999JB900149.
- Conrad, C. P., and L. Husson (2009), Influence of dynamic topography on sea level and its rate of change, *Lithosphere*, *1*(2), 110–120, doi:10.1130/L32.1.
- Conrad, C. P., M. D. Behn, and P. G. Silver (2007), Global mantle flow and the development of seismic anisotropy: Differences between the oceanic and continental upper mantle, *J. Geophys. Res.*, *112*, B07317, doi:10.1029/2006JB004608.
- Creager, K. C., and T. H. Jordan (1986), Slab penetration into the lower mantle beneath the Mariana and other island arcs of the northwest Pacific, *J. Geophys. Res.*, *91*(B3), 3573–3589, doi:10.1029/JB091iB03p03573.
- Davies, G. F. (1995), Penetration of plates and plumes through the mantle transition, *Earth Planet. Sci. Lett.*, *133*, 507–516, doi:10.1016/0012-821X(95)00039-F.
- Di Giuseppe, E., J. van Hunen, F. Fucicello, C. Faccenna, and D. Giardini (2008), Slab stiffness control of trench motion: Insights from numerical models, *Geochem. Geophys. Geosyst.*, *9*, Q02014, doi:10.1029/2007GC001776.
- Ding, X.-Y., and S. P. Grand (1994), Seismic structure of the deep Kurile subduction zone, *J. Geophys. Res.*, *99*(B12), 23,767–23,786, doi:10.1029/94JB02130.
- Engdahl, E. R., R. van der Hilst, and R. Buland (1998), Global teleseismic earthquake relocation with improved travel times and procedures for depth determination, *Bull. Seismol. Soc. Am.*, *88*(3), 722–743.
- Enns, A., T. W. Becker, and H. Schmeling (2005), The dynamics of subduction and trench migration for viscosity stratification, *Geophys. J. Int.*, *160*, 761–775, doi:10.1111/j.1365-246X.2005.02519.x.
- Faccenna, C., F. Fucicello, D. Giardini, and P. Lucente (2001), Episodic back-arc extension during restricted mantle convection in central Mediterranean, *Earth Planet. Sci. Lett.*, *187*, 105–116, doi:10.1016/S0012-821X(01)00280-1.
- Fukao, Y. (1992), Seismic tomogram of the Earth's mantle: Geodynamic implications, *Science*, *258*(5082), 625–630, doi:10.1126/science.258.5082.625.
- Fukao, Y., S. Widiyantoro, and M. Obayashi (2001), Stagnant slabs in the upper and lower mantle transition region, *Rev. Geophys.*, *39*(3), 291–323, doi:10.1029/1999RG000068.
- Fucicello, F., C. Faccenna, D. Giardini, and K. Regenauer-Lieb (2003), Dynamics of retreating slabs: 2. Insights from three-dimensional laboratory experiments, *J. Geophys. Res.*, *108*(B4), 2207, doi:10.1029/2001JB000896.
- Fucicello, F., C. Faccenna, A. Heuret, S. Lallemand, E. Di Giuseppe, and T. W. Becker (2008), Trench migration, net rotation and slab-mantle coupling, *Earth Planet. Sci. Lett.*, *271*(1–4), 233–240, doi:10.1016/j.epsl.2008.04.006.
- Gaherty, J. B., and B. H. Hager (1994), Compositional vs. thermal buoyancy and the evolution of subducted lithosphere, *Geophys. Res. Lett.*, *21*(2), 141–144, doi:10.1029/93GL03466.
- Giardini, D., and J. H. Woodhouse (1984), Deep seismicity and modes of deformation in Tonga subduction zone, *Nature*, *307*, 505–509, doi:10.1038/307505a0.
- Goes, S., F. Capitanio, and G. Morra (2008), Evidence of lower-mantle slab penetration phases in plate motions, *Nature*, *451*, 981–984.
- Grand, S. P. (1994), Mantle shear structure beneath the Americas and surrounding oceans, *J. Geophys. Res.*, *99*(B6), 11,591–11,621, doi:10.1029/94JB00042.
- Grand, S. P., R. D. Van der Hilst, and S. Widiyantoro (1997), Global seismic tomography: A snapshot of convection in the Earth, *GSA Today*, *7*, 1–7.
- Griffiths, R. W., and S. Turner (1988), Folding of viscous plumes impinging on a density or viscosity interface, *Geophys. J.*, *95*(2), 397–419, doi:10.1111/j.1365-246X.1988.tb00477.x.
- Griffiths, R. W., R. I. Hackney, and R. D. Van Der Hilst (1995), A laboratory investigation of effects of trench migration on the descent of subducted slabs, *Earth Planet. Sci. Lett.*, *133*, 1–17, doi:10.1016/0012-821X(95)00027-A.
- Gudmundsson, Ó., and M. Sambridge (1998), A regionalized upper mantle (RUM) seismic model, *J. Geophys. Res.*, *103*(B4), 7121–7136, doi:10.1029/97JB02488.
- Guillou-Frotier, L., J. Buttes, and P. Olson (1995), Laboratory experiments on the structure of subducted lithosphere, *Earth Planet. Sci. Lett.*, *133*, 19–34, doi:10.1016/0012-821X(95)00045-E.
- Hadamard, J. S. (1911), Mouvement permanent lent d'une sphere liquide et visqueuse dans un fluide visqueux, *C. R. Acad. Sci.*, *152*, 1735.
- Hager, B. H., and M. A. Richards (1989), Long wavelength variation in Earth's geoid: Physical models and dynamical implications, *Philos. Trans. R. Soc. London*, *328*, 309–327, doi:10.1098/rsta.1989.0038.
- Heuret, A., and S. Lallemand (2005), Plate motions, slab dynamics and back arc deformation, *Phys. Earth Planet. Inter.*, *149*, 31–51, doi:10.1016/j.pepi.2004.08.022.
- Houseman, G. A., and D. Gubbins (1997), Deformation of subducted oceanic lithosphere, *Geophys. J. Int.*, *131*(3), 535–551, doi:10.1111/j.1365-246X.1997.tb06598.x.
- Husson, L. (2006), Dynamic topography above retreating subduction zones, *Geology*, *34*(9), 741–744, doi:10.1130/G22436.1.
- Isacks, B., and M. Barazangi (1977), Geometry of Benioff zones: Lateral segmentation and downward bending of the subducted lithosphere, in *Island Arcs, Deep Sea Trenches and Back-Arc Basins, Maurice Ewing Ser.*, vol. 1, edited by M. Talwani and W. C. Pitman III, pp. 99–144, AGU, Washington, D. C.
- Isacks, B., and P. Molnar (1969), Mantle earthquake mechanisms and the sinking of the lithosphere, *Nature*, *223*, 1121–1124.
- Isacks, B., and P. Molnar (1971), Distribution of stresses in the descending lithosphere from a global survey of focal mechanism solutions of mantle earthquakes, *Rev. Geophys.*, *9*, 103–174, doi:10.1029/RG009i001p00103.
- Jarrard, R. D. (1986), Relations among subduction parameters, *Rev. Geophys.*, *24*, 217–284, doi:10.1029/RG024i002p00217.
- Jordan, T. H. (1977), Lithospheric slab penetration into the lower mantle beneath the Sea of Okhots, *J. Geophys.*, *43*, 473–496.
- Jordan, T. H., and W. S. Lynn (1974), A velocity anomaly in the lower mantle, *J. Geophys. Res.*, *79*, 2679–2685, doi:10.1029/JB079i017p02679.
- Káráson, H. (2002), Constraints on mantle convection from seismic tomography and flow modeling, Ph.D. thesis, Mass. Inst. of Technol., Cambridge.
- Káráson, H., and R. Van der Hilst (2001), Tomographic imaging of the lowermost mantle with differential times of refracted and diffracted core phases (PKP, Pai), *J. Geophys. Res.*, *106*, 6569–6587, doi:10.1029/2000JB900380.

- Kido, M., and O. Cadek (1997), Inferences of viscosity from the oceanic geoid: Indication of a low viscosity zone below the 660-km discontinuity, *Earth Planet. Sci. Lett.*, *151*, 125–137, doi:10.1016/S0012-821X(97)81843-2.
- Kincaid, C., and R. W. Griffiths (2003), Laboratory models of the thermal evolution of the mantle during rollback subduction, *Nature*, *425*(6953), 58–62, doi:10.1038/nature01923.
- Kincaid, C., and P. Olson (1987), An experimental study of subduction and slab migration, *J. Geophys. Res.*, *92*, 13,832–13,840.
- Kohlstedt, D. L., B. Evans, and S. J. Mackwell (1995), Strength of the lithosphere: Constraints imposed by laboratory experiments, *J. Geophys. Res.*, *100*(B9), 17,587–17,602, doi:10.1029/95JB01460.
- Lambeck, K., and P. Johnston (1998), The viscosity of the mantle: Evidence from analysis of glacial-rebound phenomena, in *The Earth's Mantle: Composition, Structure, and Evolution*, edited by I. Jackson, pp. 461–502, Cambridge Univ. Press, Cambridge, U. K.
- Lay, T. (1994), The fate of descending slabs, *Annu. Rev. Earth Planet. Sci.*, *22*, 33–61, doi:10.1146/annurev.ea.22.050194.000341.
- Li, C., R. D. van der Hilst, E. R. Engdahl, and S. Burdick (2008), A new global model for *P* wave speed variations in Earth's mantle, *Geochem. Geophys. Geosyst.*, *9*, Q05018, doi:10.1029/2007GC001806.
- Loiselet, C., L. Husson, and J. Braun (2009), From longitudinal slab curvature to slab rheology, *Geology*, *37*(8), 747–750, doi:10.1130/G30052A.1.
- Loubet, N., N. M. Ribe, and Y. Gamblin (2009), Deformation modes of subducted lithosphere at the core-mantle boundary: An experimental investigation, *Geochem. Geophys. Geosyst.*, *10*, Q10004, doi:10.1029/2009GC002492.
- Mitrovica, J. X., and A. M. Forte (2004), A new inference of mantle viscosity based upon joint inversion of convection and glacial isostatic adjustment data, *Earth Planet. Sci. Lett.*, *225*, 177–189, doi:10.1016/j.epsl.2004.06.005.
- Moresi, L., and M. Gurnis (1996), Constraints on the lateral strength of slabs from three-dimensional dynamic flow models, *Earth Planet. Sci. Lett.*, *138*, 15–28, doi:10.1016/0012-821X(95)00221-W.
- Morra, G., K. Regenauer-Lieb, and D. Giardini (2006), Curvature of oceanic arcs, *Geology*, *34*(10), 877–880, doi:10.1130/G22462.1.
- Moucha, R., A. M. Forte, J. X. Mitrovica, and A. Daradich (2007), Lateral variations in mantle rheology: Implications for convection related surface observables and inferred viscosity models, *Geophys. J. Int.*, *169*(1), 113–135, doi:10.1111/j.1365-246X.2006.03225.x.
- Müller, R., W. Roest, J. Y. Royer, L. Gahagan, and J. Sclater (1997), Digital isochrons of the world's ocean floor, *J. Geophys. Res.*, *102*, 3211–3214, doi:10.1029/96JB01781.
- Olbertz, D., M. J. R. Wortel, and U. Hansen (1997), Trench migration and subduction zone geometry, *Geophys. Res. Lett.*, *24*, 221–224, doi:10.1029/96GL03971.
- Olson, P., and H. Singer (1985), Creeping plumes, *J. Fluid Mech.*, *158*, 511–531.
- Peltier, W. R. (1996), Mantle viscosity and ice-age ice sheet tomography, *Science*, *273*, 1359–1364, doi:10.1126/science.273.5280.1359.
- Piromallo, C., and A. Morelli (2003), *P* wave tomography of the mantle under the Alpine-Mediterranean area, *J. Geophys. Res.*, *108*(B2), 2065, doi:10.1029/2002JB001757.
- Piromallo, C., T. W. Becker, F. Funicello, and C. Faccenna (2006), Three-dimensional instantaneous mantle flow induced by subduction, *Geophys. Res. Lett.*, *33*, L08304, doi:10.1029/2005GL025390.
- Puspito, N. T., Y. Yamanaka, T. Miyatake, K. Shimazaki, and K. Hirahara (1993), Three-dimensional *P* wave velocity structure beneath the Indonesian region, *Tectonophysics*, *220*(1–4), 175–192, doi:10.1016/0040-1951(93)90230-H.
- Ren, Y., E. Stutzmann, R. Van der Hilst, and J. Besse (2007), Understanding seismic heterogeneities in the lower mantle beneath the Americas from seismic tomography and plate tectonic history, *J. Geophys. Res.*, *112*, B01302, doi:10.1029/2005JB004154.
- Ribe, N. M. (2003), Periodic folding of viscous sheets, *Phys. Rev. Lett.*, *E68*, 036305.
- Ribe, N. M., E. Stutzmann, Y. Ren, and R. van der Hilst (2007), Buckling instabilities of subducted lithosphere beneath the transition zone, *Earth Planet. Sci. Lett.*, *254*(1–2), 173–179, doi:10.1016/j.epsl.2006.11.028.
- Ricard, Y., M. A. Richards, C. Lithgow-Bertelloni, and Y. Le Stunff (1993), A geodynamic model of mantle density heterogeneity, *J. Geophys. Res.*, *98*, 21,895–21,909, doi:10.1029/93JB02216.
- Royden, L. H., and L. Husson (2006), Trench motion, slab geometry and viscous stresses in subduction systems, *Geophys. J. Int.*, *167*, 881–905, doi:10.1111/j.1365-246X.2006.03079.x.
- Rybczynski, W. (1911), Über die fortschreitende Bewegung einer flüssigen Kugel in einem zähen Medium, *Bull. Acad. Sci. Cracovi. A*, *40*.
- Schellart, W. P. (2004), Kinematics of subduction and subduction-induced flow in the upper mantle, *J. Geophys. Res.*, *109*, B07401, doi:10.1029/2004JB002970.
- Schellart, W. P. (2009), Evolution of the slab bending radius and the bending dissipation in three-dimensional subduction models with a variable slab to upper mantle viscosity ratio, *Earth Planet. Sci. Lett.*, *288*, 309–319.
- Schellart, W. P., J. Freeman, D. R. Stegman, L. Moresi, and D. May (2007), Evolution and diversity of subduction zones controlled by slab width, *Nature*, *446*(7133), 308–311, doi:10.1038/nature05615.
- Spakman, W., S. van der Lee, and R. van der Hilst (1993), Travel-time tomography of the European-Mediterranean mantle down to 1400 km, *Phys. Earth Planet. Inter.*, *79*(1–2), 3–74, doi:10.1016/0031-9201(93)90142-V.
- Stegman, D. R., J. Freeman, W. P. Schellart, L. Moresi, and D. May (2006), Influence of trench width on subduction hinge retreat rates in 3-D models of slab rollback, *Geochem. Geophys. Geosyst.*, *7*, Q03012, doi:10.1029/2005GC001056.
- Tackley, P. J. (1993), Effects of strongly temperature-dependent viscosity on time-dependent, three-dimensional models of mantle convection, *Geophys. Res. Lett.*, *20*(20), 2187–2190, doi:10.1029/93GL02317.
- Tagawa, M., T. Nakakuki, and F. Tajima (2007), Dynamical modeling of trench retreat driven by the slab interaction with the mantle transition zone, *Earth Planets Space*, *59*, 65–74.
- Tajima, F., and S. P. Grand (1995), Evidence of high velocity anomalies in the transition zone associated with Southern Kurile Subduction Zone, *Geophys. Res. Lett.*, *22*(23), 3139–3142, doi:10.1029/95GL03314.
- Tajima, F., and S. P. Grand (1998), Variation of transition zone high-velocity anomalies and depression of 660 km discontinuity associated with subduction zones from the southern Kuriles to Izu-Bonin and Ryukyu, *J. Geophys. Res.*, *103*(B7), 15,015–15,036.

- Tao, W. C., and R. J. O'Connell (1993), Deformation of a weak subducted slab and variation of seismicity with depth, *Nature*, *361*(6413), 626–628, doi:10.1038/361626a0.
- Thieulot, C., P. Fullsack, and J. Braun (2008), Adaptive octree-based finite element analysis of two- and three-dimensional indentation problems, *J. Geophys. Res.*, *113*, B12207, doi:10.1029/2008JB005591.
- van der Hilst, R. (1995), Complex morphology of subducted lithosphere in the mantle beneath the Tonga trench, *Nature*, *374*(6518), 154–157, doi:10.1038/374154a0.
- van der Hilst, R., and T. Seno (1993), Effects of relative plate motion on the deep structure and penetration depth of slabs below the Izu-Bonin and Mariana island arcs, *Earth Planet. Sci. Lett.*, *120*(3–4), 395–407, doi:10.1016/0012-821X(93)90253-6.
- van der Hilst, R., and S. Widiyantoro (1997), Evidence for deep mantle circulation from global tomography, *Nature*, *386*, 578–584, doi:10.1038/386578a0.
- Vassiliou, M. S., B. H. Hager, and A. Raefsky (1984), The distribution of earthquakes with depth and stress in subducting slabs, *J. Geodyn.*, *1*(1), 11–28, doi:10.1016/0264-3707(84)90004-8.
- Wessel, P., and W. H. F. Smith (1991), Free software helps map and display data, *Eos Trans. AGU*, *72*, 441, doi:10.1029/90EO00319.
- Widiyantoro, S., and R. van der Hilst (1996), Structure and evolution of lithospheric slab beneath the Sunda Arc, Indonesia, *Science*, *271*(5255), 1566–1570, doi:10.1126/science.271.5255.1566.
- Wortel, M. J. R., and W. Spakman (2000), Subduction and slab detachment in the Mediterranean-Carpathian region, *Science*, *290*, 1910–1917, doi:10.1126/science.290.5498.1910.
- Wortel, M. J. R., and N. J. Vlaar (1988), Subduction zone seismicity and the thermo-mechanical evolution of downgoing lithosphere, *Pure Appl. Geophys.*, *128*, 625–659, doi:10.1007/BF00874551.
- Yamaoka, K. Y., Y. Fukao, and M. Kumazawa (1986), Spherical shell tectonics: Effects of sphericity and inextensibility on the geometry of the descending lithosphere, *Rev. Geophys.*, *24*, 27–53, doi:10.1029/RG024i001p00027.
- Yamato, P., L. Husson, J. Braun, C. Loiselet, and C. Thieulot (2009), Influence of surrounding plates on 3D subduction dynamics, *Geophys. Res. Lett.*, *36*, L07303, doi:10.1029/2008GL036942.
- Yoshioka, S., and M. J. R. Wortel (1995), Three-dimensional numerical modeling of detachment of subducted lithosphere, *J. Geophys. Res.*, *100*(B10), 20,223–20,244, doi:10.1029/94JB01258.
- Zhao, D., Y. Xu, D. A. Wiens, L. M. Dorman, J. Hinderbrand, and S. C. Webb (1997), Depth extent of the Lau back-arc spreading center and its relation to subduction processes, *Science*, *278*, 254–257, doi:10.1126/science.278.5336.254.
- Zhong, S., and G. F. Davies (1999), Effects of plate and slab viscosities on the geoid, *Earth Planet. Sci. Lett.*, *170*(4), 487–496, doi:10.1016/S0012-821X(99)00124-7.
- Zhong, S., and M. Gurnis (1994), Controls on trench topography from dynamic models of subducted slabs, *J. Geophys. Res.*, *99*, 15,683–15,695, doi:10.1029/94JB00809.
- Zhong, S., and M. Gurnis (1995), Mantle convection with plates and mobile, faulted plate margins, *Science*, *267*, 838–843, doi:10.1126/science.267.5199.838.
- Zhou, H.-W. (1988), How well can we resolve the deep seismic slab with seismic tomography?, *Geophys. Res. Lett.*, *15*(12), 1425–1428, doi:10.1029/GL015i012p01425.